The Astrophysical Journal, 950:167 (16pp), 2023 June 20 https://doi.org/10.3847/1538-4357/acc943

Spectroscopic Analysis of Milky Way Outer Halo Satellites: Aquarius II and Boötes II

Jordan Bruce[1], Ting S. Li[1,2], Andrew B. Pace[3], Mairead Heiger[1,2], Ying-Yi Song[1,2], and Joshua D. Simon[4]
[1] David A. Dunlap Department of Astronomy & Astrophysics, University of Toronto, 50 St. George Street, Toronto, ON M5S 3H4 Canada; ting.li@astro.utoronto.ca
[2] Dunlap Institute for Astronomy & Astrophysics, University of Toronto, 50 St. George Street, Toronto, ON M5S 3H4, Canada
[3] McWillliams Center for Cosmology, Carnegie Mellon University, 5000 Forbes Avenue, Pittsburgh, PA 15213, USA
[4] Observatories of the Carnegie Institution for Science, 813 Santa Barbara Street, Pasadena, CA 91101, USA
Received 2023 February 7; revised 2023 March 18; accepted 2023 March 23; published 2023 June 22

Abstract

In this paper, we present a chemical and kinematic analysis of two ultrafaint dwarf galaxies (UFDs), Aquarius II (Aqu II) and Boötes II (Boo II), using Magellan/IMACS spectroscopy. We present the largest sample of member stars for Boo II (12), and the largest sample of red giant branch members with metallicity measurements for Aqu II (eight). In both UFDs, over 80% of targets selected based on Gaia proper motions turned out to be spectroscopic members. In order to maximize the accuracy of stellar kinematic measurements, we remove the identified binary stars and RR Lyrae variables. For Aqu II, we measure a systemic velocity of -65.3 ± 1.8 km s^{-1} and a metallicity of $[\mathrm{Fe/H}] = -2.57^{+0.17}_{-0.17}$. When compared with previous measurements, these values display a $\sim$6 km s^{-1} difference in radial velocity and a decrease of 0.27 dex in metallicity. Similarly for Boo II, we measure a systemic velocity of $-130.4^{+1.4}_{-1.1}$ km s^{-1}, more than 10 km s^{-1} different from the literature, a metallicity almost 1 dex smaller at $[\mathrm{Fe/H}] = -2.71^{+0.11}_{-0.10}$, and a velocity dispersion 3 times smaller at $\sigma_{v_{\mathrm{hel}}} = 2.9^{+1.6}_{-1.2}$ km s^{-1}. Additionally, we derive systemic proper-motion parameters and model the orbits of both UFDs. Finally, we highlight the extremely dark-matter-dominated nature of Aqu II and compute the J-factor for both galaxies to aid searches of dark matter annihilation. Despite the small size and close proximity of Boo II, it is an intermediate target for the indirect detection of dark matter annihilation due to its low-velocity dispersion and corresponding low dark matter density.

Unified Astronomy Thesaurus concepts: Dwarf galaxies (416); Dark matter (353); Stellar kinematics (1608); Milky Way Galaxy (1054); Spectroscopy (1558); Binary stars (154)

Supporting material: machine-readable tables

1. Introduction

Ultrafaint dwarf galaxies (UFDs) are among the oldest, most metal-poor, least luminous and most dark-matter-dominated systems known (Simon 2019). They provide excellent conditions for a diverse array of research including generating or assessing models of galaxy evolution, galaxy formation, dark matter, dark matter interactions, and early universe star formation. The extremely low metallicity of these UFDs provides ideal conditions to study early universe chemical evolution (Frebel et al. 2014). With stellar ages nearly as old as the universe (Okamoto et al. 2008; Brown et al. 2012, 2014; Weisz et al. 2014; Gallart et al. 2021), UFDs provide compact and nearby examples of ancient star formation in some of the oldest galaxies, acting as relics of galaxy formation before reionization (Bovill & Ricotti 2009; Brown et al. 2012; Tarumi et al. 2021). UFDs also present many opportunities for studies related to dark matter and dark matter interactions, such as detecting dark matter annihilation and modeling dark matter distributions using resolved kinematics (Strigari 2018; Pace & Strigari 2019; Hayashi et al. 2020; Safarzadeh & Spergel 2020). Additionally, analyzing the tidal disruption of UFDs gives insight into the structure and shape of the Milky Way's dark matter halo (Bovy et al. 2016; Li et al. 2018a).

Understanding the kinematics and chemical composition of UFDs can be approached using photometry and astrometry such as in Pace et al. (2022), which prioritizes large samples of data but is limited by reduced precision. Alternatively, spectroscopy generally offers a much deeper analysis with significantly increased depth and accuracy, with the limitation of a reduced sample size of observed member stars (Li et al. 2017; Simon et al. 2017; Chiti et al. 2022; Cerny et al. 2023). Furthermore, spectroscopy can be used to gain insight into the nature of unclassified satellites as either a UFD or globular cluster (GC) through kinematic and chemical analysis. Previous spectroscopic studies of UFDs like Aquarius II (Aqu II) and Boötes II (Boo II) have been hindered by this limited sample size preventing the determination of reliable systemic properties. These two galaxies are ideal candidates for further spectroscopic study because of (i) their uncertain characteristics in the previous studies, and (ii) the large number of bright, unobserved high-probability member candidates (Pace et al. 2022). These high-probability member candidates were identified using astrometric data from the third data release (DR3) of Gaia (Gaia Collaboration et al. 2022), and could significantly improve the uncertainties in characteristics.

Aqu II was discovered by Torrealba et al. (2016) using the VLT Survey Telescope (VST), ATLAS (Shanks et al. 2015), and Sloan Digital Sky Survey (SDSS; Ahn et al. 2012) surveys and is of scientific interest due to being one of the most difficult UFDs to find. With an absolute magnitude $M_V = -4.36 \pm 0.14$ and a distance $D_\odot = 107.9 \pm 3.3$ kpc, Aqu II lies close to the current detection limit and supports the claim that there are still further and fainter UFDs yet unidentified (e.g., Drlica-Wagner et al. 2021; Mutlu-Pakdil et al. 2021). Torrealba et al. (2016) combined deep imaging with the IMACS camera on the 6.5 m Baade Telescope with spectroscopy obtained with DEIMOS on Keck to measure initial structural parameters such as the

Table 1
Observation Details

Mask	Date	MJD[a]	R.A. (h:m:s)[b]	Decl. (d:m:s)[b]	Exposure (s)	Seeing	# Observed Spectra	# Useful Spectra[c]
Aqu II	2021 June 18	59,384.35	22:33:53.079	−09:18:08.63	9600	1.″0–1.″4	55	12
Aqu II	2021 July 13	59,409.26	22:33:53.079	−09:18:08.63	4800	0.″8	55	12
Boo II	2021 June 18	59,383.80	13:57:56.000	12:50:50.00	9600	0.″8	43	17

Notes.
[a] We list the midpoint MJD of observations for each night.
[b] We list the central mask location coordinates.
[c] Useful spectra are those generating reliable velocity measurements. Most of the faintest targets do not have reliable velocity measurements due to the low S/N of the spectra.

relatively large half-light radius ($r_{1/2} = 159 \pm 24$ pc). This large half-light radius generated the initial classification of Aqu II as a dwarf galaxy since GCs never have such large sizes (GC $r_{1/2} < 20$ pc at $M_V \sim -5$; Harris 2010). Torrealba et al. (2016) also reports global properties using nine spectroscopically confirmed member stars (four red giant branch, RGB, and five blue horizontal branch, BHB, members). They measure a systemic velocity of $v_{\rm hel} = -71.1 \pm 2.5$ km s^{-1} with a dispersion of $\sigma_{v_{\rm hel}} = 5.4^{+3.4}_{-0.9}$ km s^{-1}, a metallicity of [Fe/H] $= -2.3 \pm 0.5$ (only RGB members were used for systemic metallicity), and no reported metallicity dispersion. Based on proper motion and photometric data, Pace et al. (2022) identified 15 likely Aqu II candidate member stars (with membership probability $P > 0.5$) from Gaia DR3, 12 of which have not been spectroscopically observed. Further spectroscopic investigation is therefore warranted to increase the sample size of RGB member stars, improve systemic values, and resolve a metallicity dispersion that provides insight into whether Aqu II has undergone multiple epochs of star formation.

Boo II was discovered in SDSS imaging by Walsh et al. (2007) and initially unclassified as either a UFD or GC. However, a further spectroscopic study by Koch et al. (2009) argued that Boo II was likely a UFD. Additional high-resolution spectroscopy was conducted by Koch & Rich (2014) and Ji et al. (2016b), which provided chemical evidence that supported this classification. An additional photometric study by Muñoz et al. (2018) further confirmed Boo II as a dwarf galaxy candidate due to its relatively large half-light radius ($r_{1/2} = 38.7 \pm 5.1$ pc). A photometric and spectroscopic study conducted by Koch et al. (2009) identified five member stars with a systemic velocity of $v_{\rm hel} = -117 \pm 5.2$ km s^{-1}, an unexpectedly inflated dispersion of $\sigma_{v_{\rm hel}} = 10.5 \pm 7.4$ km s^{-1}, and a systemic metallicity of [Fe/H] $= -1.79 \pm 0.05$. This dispersion is extremely large compared to other UFDs with similar properties (Simon 2019). Using a photometric halo mass estimation technique, Zaritsky & Behroozi (2023) estimate the velocity dispersion to be much smaller at $\sigma_{v_{\rm hel}} = 3.4$ km s^{-1}. Ji et al. (2016b) conducted high-resolution spectroscopy of the four brightest member stars and determined that one of the member stars is a spectroscopic binary that can cause an artificially inflated velocity dispersion when considered in kinematic analysis (Pianta et al. 2022). Using the results from Ji et al. (2016b), Simon (2019) reports a systemic metallicity of [Fe/H] $= -2.79 \pm 0.08$ with a dispersion of $\sigma_{\rm [Fe/H]} < 0.35$. Despite identifying the binary star that most likely contributed to the inflated velocity dispersion, further follow-up observations are required as the limited sample size prevented an improved velocity dispersion from being measured. According to Pace et al. (2022), there are 21 likely Boo II member candidates located in Gaia DR3, of which 17 have not been spectroscopically observed.

In this paper, we use spectroscopic data from Magellan/IMACS to identify member stars and resolve systemic properties in both Aqu II and Boo II. We spectroscopically confirm the identity of eight members in Aqu II and 12 members in Boo II. These member stars are used to improve measurements of systemic characteristics and investigate orbital properties.

The paper is organized in the following way. Section 2 describes the observation process, instrumental setup, and data reduction methods. Section 3 describes the processes used to identify members and determine radial velocities and metallicities. Section 4 discusses the scientific results and conducts an orbit analysis of the two satellites. Section 5 summarizes the findings and concludes the paper. Throughout the paper, unless specified otherwise, we use the astrometric data from Gaia DR3 (Gaia Collaboration et al. 2022) and photometric data from the Dark Energy Camera Legacy Survey (DECaLS) Data Release 9 (DR9; Dey et al. 2019). The photometry is dereddened using the color excess $E(B-V)$ from Schlafly & Finkbeiner (2011) multiplied by the extinction coefficients $R_g = 3.186$ and $R_r = 2.140$ (DES Collaboration et al. 2018).

2. Observations and Data

2.1. Observation Details

Observations were taken using the IMACS spectrograph (Dressler et al. 2011) on the Magellan-Baade Telescope, in Chile, on 2021 June 18 and July 13. Following the instrument setup outlined in Simon et al. (2017) and Li et al. (2017), we used the $f/4$ camera to attain a 15.′4 by 7′ field of view, coupled with the 1200 ℓ mm^{-1} grating, tilted at an angle of 32.4°, and a WB5600-9200 filter. This setup provided a resolution of $R \sim$11,000 for the 0.″7 $\times$5″ slit size used. The wavelength range 7550–8750 Å was chosen to adequately cover the calcium triplet (CaT) absorption lines (∼8500 Å) used to measure the radial velocities and metallicities of target stars, and the telluric A-band absorption lines (∼7600 Å) used to correct for spectral shifts resulting from a miscentering of stars within their slits.

The observations included four 2400 s science exposures each for Aqu II and Boo II on June 18 with an average seeing of ∼1.″1, and two 2400 s science exposures for Aqu II on July 13 with an average seeing of 0.″8 (refer to Table 1). Following the methods detailed in Li et al. (2017), a wavelength calibration frame and a flat-field frame were captured immediately following each pair of science exposures. For

wavelength calibration, we used He, Ne, and Ar comparison lamps as well as a Kr lamp, which has strong lines in the region neighboring the telluric absorption lines (Li et al. 2017).

We selected the targets from three categories. First, we selected all member candidates with membership probability $P > 0.2$ from Pace et al. (2022) as the highest-priority targets. We then picked other possible member candidates whose proper motions are consistent with the UFDs (but are not included in Pace et al. 2022) as the next priority. Finally, we included fainter candidates in DECaLS guided by an old metal-poor Dartmouth isochrone (Dotter et al. 2008) as the lowest-priority targets, whose astrometric information is not available in Gaia. We designed one slit mask for each UFD, placing the center and slit position angle of the mask that maximized the number of targets in the highest-priority category. In total, we selected 55 stars for Aqu II and 43 stars for Boo II. However, we note that many of the targets are in the lowest priority, with no Gaia data available. Due to the low signal-to-noise ratio (S/N) on these faint targets, we were not able to obtain good velocity measurements for stars in the lowest category, returning a low number in the useful spectra in Table 1.

2.2. Data Reduction

The IMACS spectra were reduced following the methods outlined in Li et al. (2017). This process involves subtracting bias, removing read-out pattern noise, and using the COSMOS reduction pipeline (Dressler et al. 2011; Oemler et al. 2017) to map the slits and generate a precursory wavelength solution. We then generated an enhanced wavelength calibration and spectral extraction using an IMACS pipeline (Simon et al. 2017) derived from the DEEP2 data reduction pipeline (Cooper et al. 2012). Each set of science exposures was uniquely reduced, resulting in extracted 1D spectra that were combined using a weighted average to attain the final coadded spectra for each night. These spectra were subsequently normalized to unity by fitting a quadratic polynomial. For the 55 Aqu II targets and 43 Boo II targets, 52 and 39 spectra were extracted, respectively, with several stars falling into a chip gap. The complete observation and slit mask details are outlined in Table 1.

3. Analysis

3.1. Radial Velocities

We determined stellar radial velocities following the methods detailed in Li et al. (2017), fitting a set of templates to the reduced spectra using emcee, a Markov Chain Monte Carlo (MCMC) sampler (Foreman-Mackey et al. 2013). Three spectral templates were fit for each star: the metal-poor RGB star HD 122563, the BHB star HD 161817, and the moderately metal-poor RGB star HD 26297. Each template was shifted through a range of velocities to find the radial velocity, $v_{\rm rad}$, value that maximized the log-likelihood function:

$$\log L = -\frac{1}{2}\Sigma_{\lambda=\lambda_1}^{\lambda_2}\frac{\left[S(\lambda) - T(\lambda(1+\frac{v_{\rm rad}}{c}))\right]^2}{\sigma_{\rm spec}^2(\lambda)}. \quad (1)$$

Above, $S(\lambda)$ and $\sigma_{\rm spec}^2(\lambda)$ reflect the normalized spectrum and its variance, and $T(\lambda(1-\frac{v_{\rm rad}}{c}))$ represents the normalized template. The wavelength bounds of the fit were set as $\lambda_1 = 8450$ Å to $\lambda_2 = 8685$ Å since the CaT spectral feature was predominantly used to measure radial velocity.

For each star, we ran the MCMC sampler with 20 walkers each making 1000 steps and a burn-in stage of 50 steps, which was omitted. We then removed 5σ outliers, and report the median and standard deviation of the posterior distributions as the radial velocity ($v_{\rm rad}$) and its error ($\sigma_{v_{\rm rad}}$), respectively.

Next, we measured and applied a telluric correction, $v_{\rm tell}$, to account for radial-velocity shifts arising from a miscentering of stars within their slits. The MCMC sampler was run again using the methods previously described, using a telluric template of the hot, rapidly rotating star HR 4781 (Simon et al. 2017) over the range $\lambda_1 = 7550$ Å to $\lambda_2 = 7700$ Å. Similarly, the median and standard deviation of the posterior distribution are reported as the telluric correction ($v_{\rm tell}$) and its uncertainty ($\sigma_{v_{\rm tell}}$), respectively. For the first epoch of Aqu II the telluric corrections ranged from -5.3 to -2.7 km s^{-1}, with uncertainties ranging from 0.2 to 2.0 km s^{-1}. In the second epoch the telluric corrections ranged from -4.5 to -0.8 km s^{-1}, with uncertainties ranging from 0.1 to 1.8 km s^{-1}. For Boo II the telluric corrections ranged from -2.4 to 0.6 km s^{-1}, with uncertainties ranging from 0.1 to 1.9 km s^{-1}. Since there was no dramatic trend in the corrections of high S/N spectra, we adopted an average telluric correction for low S/N outliers that significantly deviated from the other corrections.

The observed radial velocity (v) was measured by subtracting the A-band correction, $v = v_{\rm rad} - v_{\rm tell}$. We note that $\sigma_{v_{\rm rad}}$ and $\sigma_{v_{\rm tell}}$ are solely statistical and uniquely associated with the measurements and S/N of the 1D spectra. We also include a systematic uncertainty, $\sigma_{\rm sys}$, of 1.0 km s^{-1}, previously identified in Li et al. (2017) and Simon et al. (2017), by comparing multiple successive IMACS observations using similar instrumental setups. The total velocity uncertainty is defined as the square root of the sum of the squares, $\sigma_v = \sqrt{\sigma_{v_{\rm rad}}^2 + \sigma_{v_{\rm tell}}^2 + \sigma_{\rm sys}^2}$.

Aqu II was observed on two epochs, 2021 June 18 and 2021 July 13, respectively. The two epochs are far enough apart that the heliocentric corrections from the two epochs are significantly different. Considering the low S/N property of the data, we performed a joint fit with data from both epochs. The radial-velocity templates were simultaneously fit to spectra from each night, and the MCMC sampler was run as previously described. We measured the observed velocity as the velocity that generated the largest overall likelihood from Equation (1) on both nights combined. Individual telluric corrections were applied for each spectrum prior to the simultaneous fitting, and the median and standard deviation of the combined posterior distribution are reported as the observed radial velocity ($v_{\rm rad}$) and its error ($\sigma_{v_{\rm rad}}$), respectively. The statistical uncertainties were similarly summed in quadrature, $\sigma_{v_{\rm stat}} = \sqrt{\sigma_{v_{\rm tell,\ June\ 18}}^2 + \sigma_{v_{\rm tell,\ July\ 13}}^2 + \sigma_{v_{\rm rad}}^2}$, along with the systemic uncertainty from Li et al. (2017) and Simon et al. (2017), $\sigma_v = \sqrt{\sigma_{v_{\rm stat}}^2 + \sigma_{v_{\rm sys}}^2}$.

We note that an S/N cut of 2.0 was applied to our set of spectra as the large amount of noise prevents an accurate template fitting. This reduction, as well as visual inspection to remove imprecise measurements, resulted in 12 and 17 useful spectra being reported for Aqu II and Boo II, respectively.

The observed radial velocities were transformed to account for a heliocentric correction based on the location of the dwarf galaxy, the time of observation, and the location of the observatory. The resulting radial velocities in the heliocentric frame, $v_{\rm hel}$, are reported in Tables 3 and 4, and hereafter

Table 2
Properties of Aquarius II and Boötes II

Property	Description	Aquarius II	Boötes II	Units
α_{2000}	R.A.	338.4813 ± 0.005[a]	209.5141 ± 0.005[b]	deg
δ_{2000}	decl.	-9.3274 ± 0.005[a]	12.8553 ± 0.006[b]	deg
r_h	Angular half-light radius	5.1 ± 0.8[a]	3.17 ± 0.42[b]	arcminutes
$r_{1/2}$	Physical half-light radius	159 ± 24[a]	38.7 ± 5.1[b]	pc
ϵ	Ellipticity	0.39 ± 0.09[a]	0.25 ± 0.11[b]	⋯
P.A.	Position angle	121 ± 9[a]	-68 ± 27[b]	deg
$m - M$	Distance modulus	20.16 ± 0.07[a]	18.12 ± 0.06[b]	mag
$D_\odot$	Distance (heliocentric)	107.9 ± 3.3[a]	42.0 ± 2.0[b]	kpc
M_v	Absolute magnitude (V band)	-4.36 ± 0.14[a]	-2.9 ± 0.7[b]	mag
$N_{\rm reported}$	Number of observed members	8	12	⋯
$E(B-V)$	Average reddening	0.07[c]	0.03[c]	mag
$v_{\rm hel}$	Systemic velocity (heliocentric)	-65.3 ± 1.8	$-130.4^{+1.4}_{-1.1}$	km s^{-1}
$\sigma_{v_{\rm hel}}$	Velocity dispersion	$4.7^{+1.8}_{-1.2}$	$2.9^{+1.6}_{-1.2}$	km s^{-1}
[Fe/H]	Systemic metallicity	$-2.57^{+0.17}_{-0.17}$	$-2.71^{+0.11}_{-0.10}$	dex
$\sigma_{\rm [Fe/H]}$	Metallicity dispersion	$0.36^{+0.20}_{-0.14}$	<0.37	dex
$M_{1/2}$	Dynamical mass inside $r_{1/2}$	$3.1^{+3.0}_{-1.4} \times 10^6$	$3.1^{+4.4}_{-2.1} \times 10^5$	$M_\odot$
$M_{1/2}/L_{v,1/2}$	Mass-to-light ratio	1300^{+1300}_{-600}	460^{+1000}_{-440}	$M_\odot/L_\odot$
μ_α	Systemic proper motion in R.A.	-0.27 ± 0.12	-2.50 ± 0.07	mas yr^{-1}
μ_δ	Systemic proper motion in decl.	-0.44 ± 0.10	-0.46 ± 0.06	mas yr^{-1}
$r_{\rm apo}$	Orbit apocenter	148^{+119}_{-35}	203^{+61}_{-56}	kpc
$r_{\rm peri}$	Orbit pericenter	96^{+7}_{-35}	38^{+1}_{-2}	kpc
e	Orbit eccentricity	$0.30^{+0.20}_{-0.11}$	$0.69^{+0.06}_{-0.08}$	⋯
$r_{\rm apo}^{\rm LMC}$	Orbit apocenter (with LMC)	158^{+126}_{-38}	198^{+58}_{-50}	kpc
$r_{\rm peri}^{\rm LMC}$	Orbit pericenter (with LMC)	96^{+7}_{-30}	40^{+5}_{-4}	kpc
$e^{\rm LMC}$	Orbit eccentricity (with LMC)	$0.32^{+0.18}_{-0.08}$	$0.67^{+0.05}_{-0.07}$	⋯
$\log_{10} J(0.^\circ 2)$	Integrated J-factor within a solid angle of 0.2°	$17.7^{+0.6}_{-0.5}$	$18.1^{+0.8}_{-1.1}$	GeV^2 cm^{-5}
$\log_{10} J(0.^\circ 5)$	Integrated J-factor within a solid angle of 0.5°	$17.8^{+0.6}_{-0.5}$	$18.3^{+0.8}_{-1.1}$	GeV^2 cm^{-5}

Notes.
[a] Most recent measurements reported in the Aqu II discovery paper (Torrealba et al. 2016).
[b] Most recent measurements for Boo II reported in the 2018 photometric study by Muñoz et al. (2018).
[c] The reddening was computed using the average of individual star reddening based on values from Schlafly & Finkbeiner (2011).

referred to as the stellar velocity. Table 3 presents the velocity measurements of the observed stars for Aqu II, while Table 4 displays the velocity measurements of the observed stars for Boo II. Our observations of Aqu II resulted in velocities for 12 stars to be computed, eight of which were identified as member stars. Seventeen stars were observed with good velocity measurements during the Boo II exposures, 12 of which were identified to be members.

3.2. Metallicity Measurements

We determined metallicities of RGB stars using the equivalent widths (EWs) of the CaT absorption lines. Following the method described in Li et al. (2017) and Simon et al. (2017), we uniquely measured the EW of each CaT line by fitting a Gaussian plus Lorentzian function. We then converted the summed EWs and absolute V-band magnitude of each star into metallicity ([Fe/H]) using a well-defined conversion relation from Carrera et al. (2013). Using photometry from DECaLS, the dereddened g-band (g_0) and r-band (r_0) magnitudes for each star were converted into apparent V-band magnitude using Equation (5) from Bechtol et al. (2015), using the distance modulus from previous studies (Table 2). We determined the metallicity generated from the conversion relation in Carrera et al. (2013), with the uncertainties measured by summing the statistical and systemic uncertainties in quadrature as outlined in Li et al. (2017). The statistical uncertainty stems primarily from the Gaussian plus Lorentzian fitting, along with uncertainty in the DECaLS DR9 photometry and distance modulus, which are all propagated through the conversion relation. Uncertainties in the relation parameters as outlined in Carrera et al. (2013) are also included. A systematic uncertainty of 0.2 Å in EWs was also incorporated as determined from repeat measurements in Li et al. (2017).

Target selection prioritized potential RGB members, resulting in the majority of member stars providing metallicity measurements. An S/N cut of 2.0 was made for spectra once again, and the EW fit of each CaT line was visually inspected to remove stars with bad fitting. For Aqu II, when both epochs produced verified metallicities a weighted average is reported. In the case of two stars (Gaia DR3 source IDs: 2609061687357323776 and 2609107798126218880) only the first epoch provided accurate measurements, preventing a weighted average from being determined. Visual inspection yielded eight RGB stars with good-fit EW measurements in Aqu II observations, and eight in Boo II observations. Since the metallicity relation relies on the distance modulus and solely applies to RGB stars, we only report the metallicity of RGB member stars in each UFD. The metallicity values for Aqu II members are listed in Table 3, while the metallicity values for Boo II members are listed in Table 4.

Table 3
Aquarius II Observed Spectra

Gaia DR3 Source ID	R.A. (deg)	Decl. (deg)	g_0 (mag)	r_0 (mag)	S/N 1[a]	S/N 2[a]	v_{hel} (km s^{-1})	EW 1[a]	EW 2[a]	[Fe/H] (dex)	Member[b]
2609060660860398208	338.57394	−9.35700	20.58	19.94	3.8	3.5	56.6 ± 2.3	⋯	⋯	⋯	NM
2609061068882022784	338.52885	−9.35453	20.22	19.61	5.4	6.1	−85.0 ± 1.6	⋯	⋯	⋯	NM
2609061141896425088	338.49945	−9.36063	20.77	20.18	3.3	3.3	−126.0 ± 3.5	⋯	⋯	⋯	NM
2609061687357323776	338.53523	−9.32780	19.32	18.54	15.5	13.4	−66.7 ± 1.2	4.74 ± 0.39	⋯	−1.87 ± 0.18	M
2609061760371960704	338.52684	−9.32317	19.58	18.91	11.0	10.2	−64.2 ± 1.3	2.17 ± 0.41	2.13 ± 1.27	−2.92 ± 0.22	M
2609107798126218880	338.39674	−9.31998	20.53	19.95	3.7	3.7	−71.8 ± 2.8	1.47 ± 1.00	⋯	−3.13 ± 0.73	M
2609107935565172224	338.36675	−9.32105	20.08	19.45	5.8	6.6	−60.2 ± 1.8	3.55 ± 1.34	3.75 ± 1.08	−2.12 ± 0.37	M
2609108588400203264	338.46083	−9.31525	20.11	19.51	5.8	5.8	−69.6 ± 2.0	1.85 ± 0.57	1.92 ± 0.40	−2.95 ± 0.21	M
2609109756631321472	338.46956	−9.28585	19.25	18.54	15.9	13.8	−57.1 ± 1.2	3.29 ± 0.42	2.94 ± 0.36	−2.56 ± 0.14	M
2609113055166221056	338.42154	−9.25084	16.79	16.67	40.3	31.3	−57.4 ± 1.1	⋯	⋯	⋯	NM
2609155489443129088	338.59370	−9.30185	18.81	18.02	23.2	18.9	−68.5 ± 1.1	3.08 ± 0.25	2.92 ± 0.33	−2.70 ± 0.11	M
2609202665363907328	338.55648	−9.28793	19.46	18.78	12.6	9.9	−66.2 ± 1.3	2.59 ± 0.40	2.52 ± 0.14	−2.76 ± 0.11	M

Notes. Astrometry and source IDs are taken from Gaia DR3, and the photometry is taken from LS DR9 (DECaLS). The S/N ratio refers to the spectra observed with the IMACS data.
[a] "EW 1" refers to the equivalent width measurements of the CaT lines from the first epoch of observations (2021 June 18). "EW 2" refers to the equivalent width measurements of the CaT lines from the second epoch of observations (2021 July 13). Similarly, "S/N 1" and "S/N 2" refer to the S/N of the spectra from the first and second epochs, respectively.
[b] "M" refers to confirmed member stars, "NM" are confirmed nonmember stars.

(This table is available in machine-readable form.)

Table 4
Boötes II Observed Spectra

Gaia DR3 Source ID	R.A. (deg)	Decl. (deg)	g_0 (mag)	r_0 (mag)	S/N	v_{hel} (km s^{-1})	EW	[Fe/H] (dex)	Member[a]
3727825076541007232	209.43238	12.79053	20.20	19.70	7.6	-126.9 ± 2.2	2.79 ± 1.44	-2.03 ± 0.74	M
3727825145260749952	209.41684	12.80064	22.32	20.94	6.0	-17.6 ± 2.3	⋯	⋯	NM
3727825488857874816	209.45241	12.80229	20.82	20.44	3.3	110.6 ± 6.6	⋯	⋯	NM
3727826283427161728	209.50698	12.82085	20.64	20.19	4.4	-128.4 ± 2.9	⋯	⋯	M
3727826004253947776	209.54107	12.79852	20.28	19.79	5.8	-130.2 ± 2.3	1.43 ± 0.78	-2.82 ± 0.63	M
3727826111628452224	209.53242	12.82263	20.66	20.18	4.1	-120.7 ± 3.1	2.44 ± 1.92	-2.12 ± 1.04	M
3727826141692913792	209.55987	12.82006	21.02	20.72	2.4	29.8 ± 5.3	⋯	⋯	NM
3727837587781240320	209.41683	12.84375	20.62	20.43	2.6	98.8 ± 4.5	⋯	⋯	NM
3727837759579718272	209.40610	12.86346	18.14	17.63	35.0	-134.0 ± 1.0	1.89 ± 0.04	-2.93 ± 0.13	M
3727825901174760832	209.44692	12.84726	20.97	20.42	3.5	-26.4 ± 5.5	⋯	⋯	NM
3727827382938924800[b]	209.46324	12.86025	19.12	18.59	18.6	-134.9 ± 1.2	2.22 ± 0.14	-2.55 ± 0.14	M
3727827516082474880	209.48409	12.86877	19.37	18.85	14.8	-131.5 ± 1.3	1.78 ± 0.46	-2.75 ± 0.32	M
3727827241204558720	209.50591	12.85140	19.43	18.92	14.7	-130.5 ± 1.3	1.66 ± 0.10	-2.82 ± 0.16	M
3727839301472744192	209.44428	12.89235	20.25	19.74	6.5	-130.0 ± 2.3	2.83 ± 0.77	-2.00 ± 0.40	M
3727826519650056576[c]	209.52933	12.85634	18.71	18.23	18.3	-118.4 ± 1.4	⋯	⋯	M
3727826519650056832[d]	209.53947	12.85719	20.31	19.86	6.0	-138.5 ± 2.6	⋯	⋯	M
3727826657089011840	209.57290	12.86183	20.32	19.83	5.5	-135.8 ± 2.4	⋯	⋯	M

Notes. Astrometry and source IDs are taken from Gaia DR3, and the photometry is taken from LS DR9 (DECaLS). The S/N ratio refers to the spectra observed with the IMACS data.
[a] "M" refers to confirmed member stars, "NM" are confirmed nonmember stars.
[b] The binary star identified in Ji et al. (2016b).
[c] The RR Lyrae star located in the Gaia DR3 RR Lyrae star catalog (Clementini et al. 2022).
[d] The potential binary star identified due to variation in observed velocity measurements between Koch et al. (2009) and this work.

(This table is available in machine-readable form.)

3.3. Determining Membership

For each dwarf the membership status of the observed stars was determined by examining their location on a color–magnitude diagram (CMD), spatial position, proper motion, and velocity. We use DECaLS DR9 photometry, with proper motion and astrometry retrieved through a positional cross-match with Gaia DR3. By jointly analyzing these parameters, the observed members were distinctly identified.

In Figure 1, we compare the chemical and kinematic properties of all stars observed during the Aqu II observations. Of the 12 useful Aqu II spectra, nine stars comprise a velocity grouping between -55 km s^{-1} and -70 km s^{-1}, consistent with the expected velocity from Torrealba et al. (2016). Of these potential members, eight are tightly grouped in proper-motion space, located within 2 half-light radii (r_h) of the observed center, and lie along the projected Dartmouth isochrone (Dotter et al. 2008) plotted using the reported distance modulus from Torrealba et al. (2016), a metallicity of [Fe/H] $= -2.49$, and an age of 12.5 Gyr. We note that one member star slightly deviates from the isochrone (Gaia DR3 source ID: 2609061687357323776). This star's redder color may be due to a high carbon abundance causing excess absorption in blue bands. We also note the velocity-consistent nonmember (Gaia DR3 source ID: 2609113055166221056) that is located $>3\sigma$ away from the clustering in proper-motion space, and therefore is not a member. This nonmember is also not included in the high-probability sample from Pace et al. (2022), since the parallax was nonzero at 3σ (parallax $-$ 3×parallax_error > 0).

In Figure 2, we compare the chemical and kinematic properties of all stars observed during the Boo II observations. Of the 17 useful Boo II spectra, 12 stars form a clear velocity grouping between -115 km s^{-1} and -140 km s^{-1}, resulting in the five remaining stars being immediately classified as nonmembers. These 12 candidates were similarly grouped near the center of Boo II in position space, along the projected isochrone, and within 1–2σ of each other in proper-motion space. We therefore classify these 12 stars as members of Boo II. We note that, in addition to the RR Lyrae (RRL) member, there is another star that deviates from the isochrone (Gaia DR3 source ID: 3727837759579718272) and there is a possibility that this star is a nonmember based on this offset in photometry. As discussed later, in Section 4.1, when this star is removed the velocity dispersion decreases from $\sigma_{v_{hel}} = 2.9^{+1.6}_{-1.2}$ km s^{-1} to $\sigma_{v_{hel}} = 1.3^{+2.3}_{-1.3}$ km s^{-1}. However, we still consider the star a member due to its extremely metal-poor nature ([Fe/H] ∼–3) and close proximity in proper motion, position, and velocity plots (Figure 2).

One Boo II member star (Gaia DR3 source ID: 3727826519650056576) is in the Gaia DR3 RRL catalog (Clementini et al. 2022). This star is outlined in green in Figure 2 and its characteristics are detailed in Table 5. This star is reported as a member but it is excluded from calculations determining systemic radial velocity and velocity dispersion in Section 4.1, as well as metallicity and metallicity dispersion in Section 4.1.

We also highlight the presence of two binary stars in Boo II (Gaia DR3 source IDs: 3727827382938924800 and 3727826519650056832), which are similarly detailed in Table 5. The first binary star (binary star 1 in this work and BooII-15 in Koch et al. 2009) was first identified by Ji et al. (2016b) using high-resolution spectroscopy and is outlined in cyan in Figure 2. The second binary star (binary star 2 in this work and BooII-3 in Koch et al. 2009) is outlined in black in Figure 2. This second binary star was identified when we noticed the velocity from the Koch et al. (2009) sample differed from this work by 29.1 ± 8.0 km s^{-1}. This large variation in velocity indicates its likely identity as a binary star. Both of these stars are excluded from kinematic analysis to prevent an artificial inflation of the velocity dispersion or a shift in systemic velocity measurements.

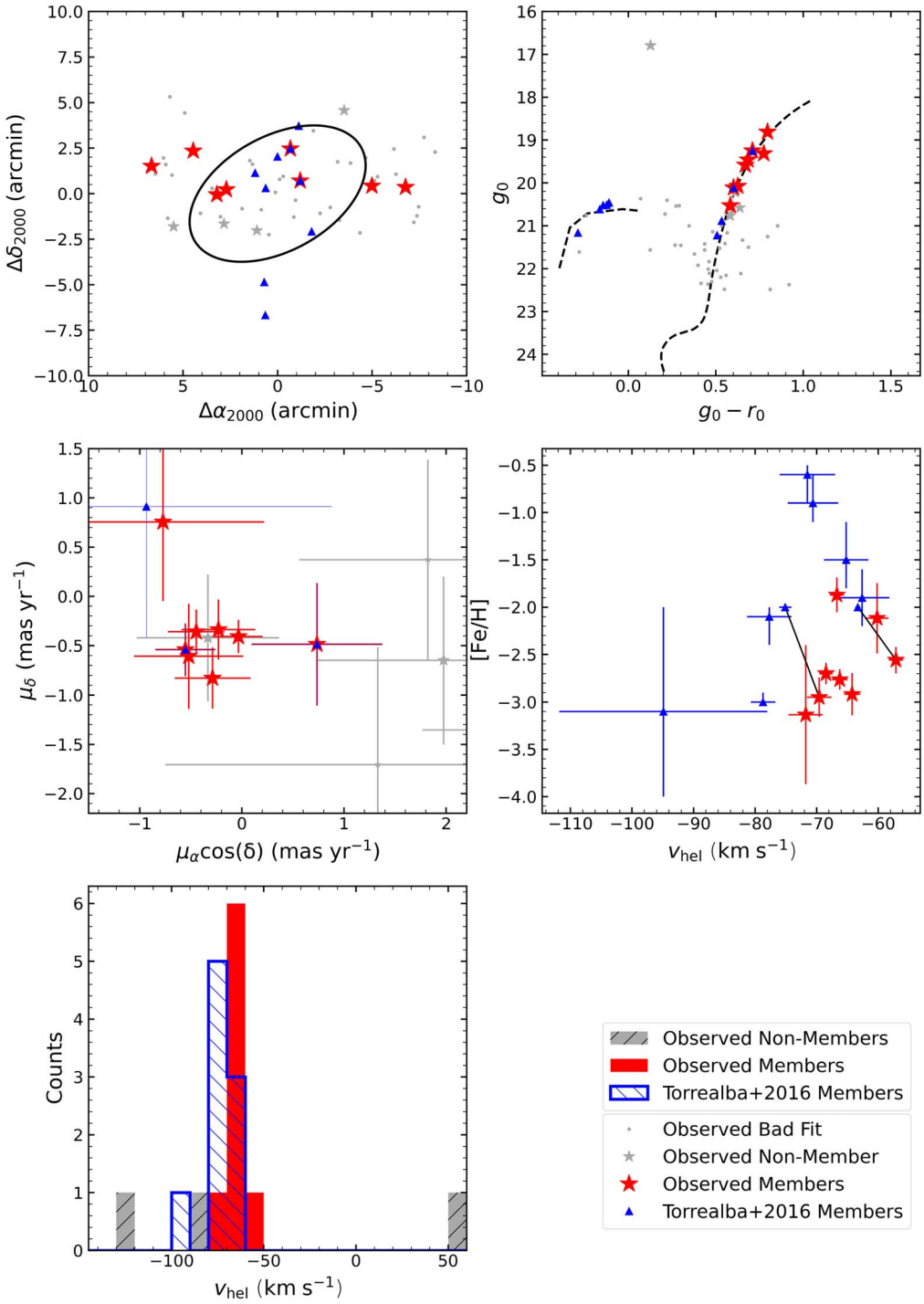

Figure 1. Top left: spatial position of 55 observed stars and nine member stars from Torrealba et al. (2016) for Aqu II. The dashed ellipse displays the half-light radius plotted using the ellipticity, P.A., and r_h from Torrealba et al. (2016). Top right: color–magnitude diagram displaying a Dartmouth isochrone (Dotter et al. 2008) with an age of 12.5 Gyr and a metallicity of [Fe/H] = –2.49 plotted using the distance modulus of 20.16 from Torrealba et al. (2016). Middle left: proper-motion distribution using Gaia DR3 data (Gaia Collaboration et al. 2016, 2021; Lindegren et al. 2021) for stars when available. Middle right: velocity (v_{hel}) and metallicity ([Fe/H]) distribution, with black lines connecting identical stars observed in this work and Torrealba et al. (2016). Bottom left: histogram of observed velocities (v_{hel}) and Torrealba et al. (2016) velocities.

From the above analysis, we confirm eight Aqu II members and 12 Boo II members (three of which are excluded from kinematic analysis). These member stars are unambiguous in their classification due to tightly grouped locations in position, velocity, metallicity, proper motion, and color–magnitude diagrams.

Among the 10 (13) high-probability member candidates ($P > 0.5$ in Pace et al. 2022, using the `mem_fixed` column) we observed in Aqu II (Boo II), eight (11) are confirmed to be members. Only two (two) are nonmembers in these galaxies. This shows that the proper motions and astrometric information from Gaia largely improved the target-selection efficiency. We note that there remain five high-probability member candidates in Aqu II[5]

[5] Gaia DR3 source IDs for additional high-probability member candidates in Aqu II: 2609057770347087104, 2609059179096375808, 2609059213456115584, 2609100170264245376, 2609108760198902144.

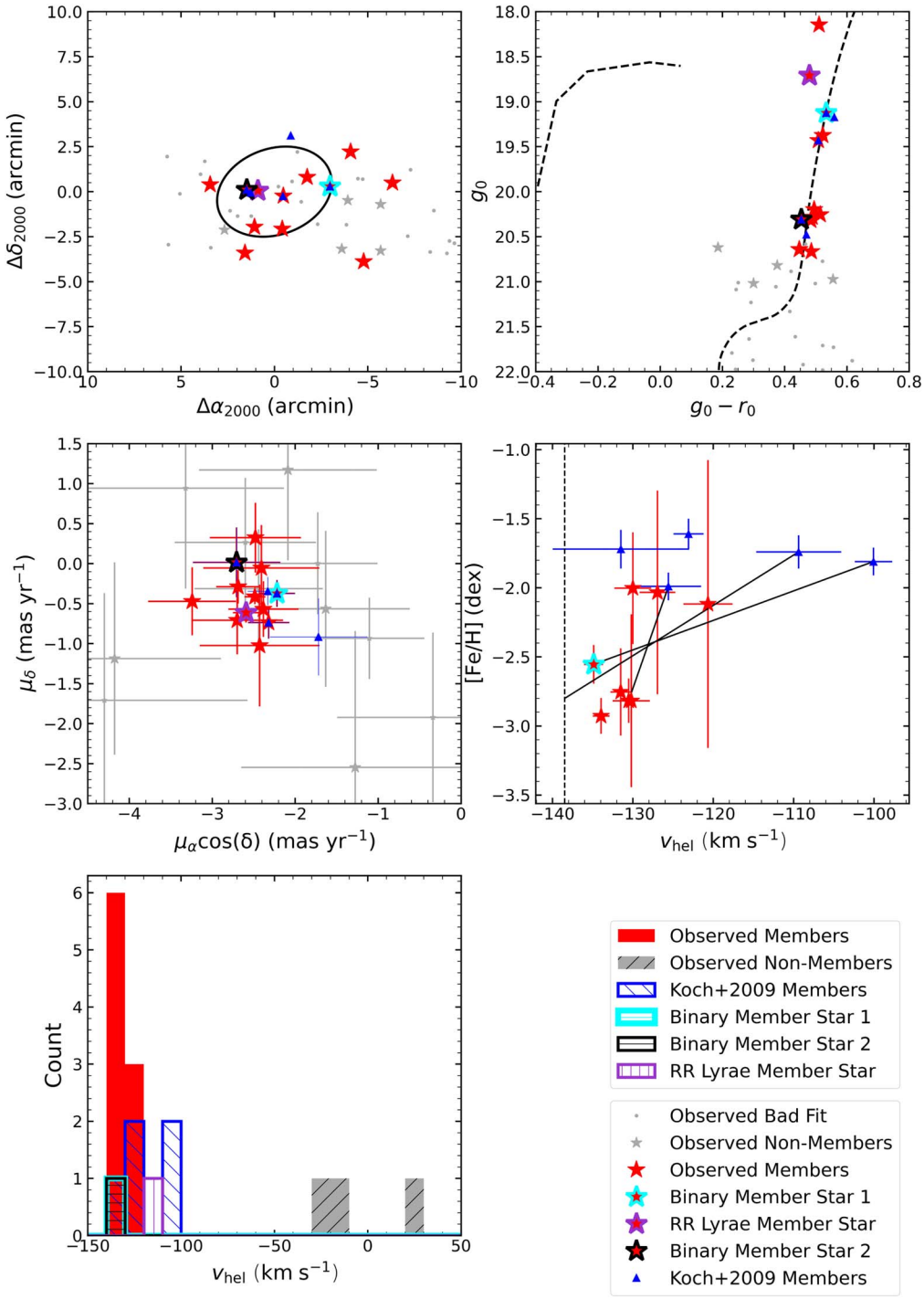

Figure 2. Top left: spatial position of 43 observed stars and five member stars from Koch et al. (2009) for Boo II. The dashed ellipse displays the half-light radius plotted using the ellipticity, P.A., and r_h from Muñoz et al. (2018). Top right: color–magnitude diagram displaying a Dartmouth isochrone (Dotter et al. 2008) with an age of 12.5 Gyr and a metallicity of [Fe/H] = −2.49 plotted using the distance modulus of 18.12 from Walsh et al. (2008). Middle left: proper-motion distribution using Gaia DR3 data (Gaia Collaboration et al. 2016, 2021; Lindegren et al. 2021) for stars when available. Middle right: velocity ($v_{\rm hel}$) and metallicity ([Fe/H]) distribution of members from this work and Koch et al. (2009) with well-fit metallicity measurements, with black lines connecting stars observed in both studies. The black vertical line represents binary member star 2, which had a low S/N ratio that prevented accurate metallicity measurements. Bottom left: histogram of observed velocity ($v_{\rm hel}$) and Koch et al. (2009) velocities. Binary star 1 refers to the binary identified by Ji et al. (2016b), whereas binary star 2 refers to the suspected binary identified in this work.

and eight in Boo II[6] that either we did not observe due to slit conflicts in the mask design, or we observed but could not obtain $v_{\rm hel}$ due to the low S/N of the spectra. These stars should be prioritized in future observations to complete the sample of Gaia members in these two dwarf galaxies. We also note that for the RRL star in Boo II (Gaia DR3 source ID: 3727826519650056576) we confirmed its membership despite the fact that it was not included in the high-probability member candidates list from Pace et al. (2022). This star was not

[6] Gaia DR3 source IDs for additional high-probability member candidates in Boo II: 3727823118035927936, 3727826107333175936, 3727826416570828800, 3727826519650055168, 3727827309924042624, 3727827997118825856, 3727835075224948352, 3727837239888417792.

Table 5
Binary and RR Lyrae Stars in Boo II

ID	$v_{\rm hel}$ (km s^{-1})[a]	$v_{\rm hel}$ (km s^{-1})[b]	$v_{\rm hel}$ (km s^{-1})[c]	$v_{\rm hel}$ (km s^{-1})[d]	Classification
3727826519650056576	⋯	-118.4 ± 1.4	⋯	⋯	RR Lyrae star
3727827382938924800	-100.07 ± 2.33	-130.5 ± 1.3	-104.8	~ -120	Binary star (Ji+2016)
3727826519650056832	-109.38 ± 5.28	-138.5 ± 2.7	⋯	⋯	Suspected binary star

Notes.
[a] Values taken from Koch et al. (2009). Observations occurred on 2007 April 17.
[b] Values from this work. Observations occurred on 2021 June 18.
[c] Values taken from Koch & Rich (2014). Observations occurred on 2014 May 23.
[d] Values taken from Ji et al. (2016b). Observations occurred on 2014 March 21 and 2015 June 17–18.

considered in the input data for the modeling in Pace et al. (2022) due to it failing an uncommon Gaia flag (`ipd_gof_harmonic_amplitude` > 0.1).

4. Discussion

In this section, we evaluate the systemic properties of Aqu II and Boo II. We consider the global velocity dispersions, metallicity dispersions, and orbital characteristics, as well as investigate the dark matter annihilation.

4.1. Velocity and Metallicity Dispersion

With eight and nine (excluding RRL and binary stars) spectroscopically confirmed members of Aqu II and Boo II, we evaluate the systemic velocity and its dispersion following the methods in Li et al. (2017). Similarly, we use the eight and 11 (excluding the RRL star) spectroscopically confirmed members of Aqu II and Boo II to measure the systemic metallicity and its dispersion. We use a two-parameter Gaussian likelihood function (Equation (2) from Li et al. 2017), derived from Walker et al. (2006). Using emcee (Foreman-Mackey et al. 2013), an MCMC sampler was run to sample this Gaussian using 50 walkers making 1000 steps with an additional burn-in period of 100 steps. The systemic velocity or metallicity is determined as the median of the respective posterior distribution, with uncertainties derived from the 16th and 84th percentiles.

In Figure 3, we determine the systemic velocity, metallicity, and the respective dispersions for Aqu II. Using the eight observed Aqu II members, we measure a systemic velocity of $v_{\rm hel} = -65.3 \pm 1.8$ km s^{-1} and a dispersion of $\sigma_{v_{\rm hel}} = 4.7^{+1.8}_{-1.2}$ km s^{-1}. The systemic metallicity is measured as $[{\rm Fe/H}] = -2.57^{+0.17}_{-0.17}$ with a dispersion of $\sigma_{[{\rm Fe/H}]} = 0.36^{+0.20}_{-0.14}$.

In Figure 4, we similarly determine the systemic velocity, velocity dispersion, metallicity, and metallicity dispersion for Boo II. The nine confirmed members of Boo II in this work (excluding RRL and binary stars) generate a systemic velocity of $v_{\rm hel} = -130.4^{+1.4}_{-1.1}$ km s^{-1} with a dispersion of $\sigma_{v_{\rm hel}} = 2.9^{+1.6}_{-1.2}$ km s^{-1}. The systemic metallicity from the eight RGB member stars in this work with well-fit metallicity measurements (excluding the RRL star but including the binary stars) is $[{\rm Fe/H}] = -2.71^{+0.11}_{-0.10}$. The metallicity dispersion of Boo II is not resolved with these eight RGB members; we instead report a 95% upper limit of $\sigma_{[{\rm Fe/H}]} < 0.37$.

As discussed in McConnachie & Côté (2010), Li et al. (2017), and Simon et al. (2017), it is possible for binary member stars to artificially inflate the velocity dispersion, especially with the small time span of observations for Boo II. To test the robustness, we performed a jackknife test for each dwarf, repeatedly removing a single star at a time to measure the effect it has on the global properties.

For Aqu II the majority of stars had minimal effects on any property of the galaxy. However, the most metal-rich star (Gaia DR3 source ID: 2609061687357323776), which was also noted to deviate from the isochrone in Section 3.3, dramatically affects the metallicity dispersion. When this star is not considered in calculations, the metallicity dispersion decreases to $\sigma_{[{\rm Fe/H}]} = 0.04^{+0.08}_{-0.02}$ (from the initial $\sigma_{[{\rm Fe/H}]} = 0.36^{+0.20}_{-0.14}$ dex) and therefore becomes unresolved. Additionally, a separate star (Gaia DR3 source ID: 2609109756631321472) significantly lowers the velocity dispersion from $\sigma_{v_{\rm hel}} = 4.7^{+1.8}_{-1.2}$ km s^{-1} to $\sigma_{v_{\rm hel}} = 2.7^{+1.6}_{-1.2}$ km s^{-1} when removed. These stars are still considered members but are noted here due to the large impacts on metallicity, metallicity dispersion, and velocity dispersion.

Similarly, for Boo II we performed a jackknife test, and we note that no star dominantly affected the systemic metallicity, metallicity dispersion, or systemic velocity (the known RRL and binary stars were not included for velocity jackknife tests). We do notice that two stars (Gaia DR3 source IDs: 3727826111628452224 and 3727837759579718272, the latter of which was the star discussed in Section 3.3 due to its deviation from the isochrone) lowered the velocity dispersion from $\sigma_{v_{\rm hel}} = 2.9^{+1.6}_{-1.2}$ km s^{-1} to $\sigma_{v_{\rm hel}} = 0.8^{+1.5}_{-0.8}$ km s^{-1} and $\sigma_{v_{\rm hel}} = 1.3^{+2.3}_{-1.3}$ km s^{-1}, respectively, when removed. These stars are still considered members but are noted here due to the large impact on the velocity dispersion.

The variation in the velocity dispersion noticed during the jackknife tests shows how one star can have a significant impact. With a limited sample size there is a possibility these stars are binaries or nonmembers, causing inflation in the velocity dispersion. However, the derived values could also purely be the true dispersions of the galaxies. For example, when we include the two binary stars in our calculations for Boo II, the velocity dispersion increases to $\sigma_{v_{\rm hel}} = 3.6^{+1.4}_{-1.1}$ km s^{-1}, which is consistent within the uncertainty but still ∼25% larger than the dispersion derived without binaries. This emphasizes the need for larger sample sizes and/or multiepoch observations to resolve this uncertainty, which could be achieved by observing the high-probability Gaia member candidates from Section 3.3 that were not included in this study.

Both dwarf galaxies are extremely metal poor (Aqu II $[{\rm Fe/H}] = -2.57^{+0.17}_{-0.17}$; Boo II $[{\rm Fe/H}] = -2.71^{+0.11}_{-0.10}$), placing them among the lowest known UFD metallicities alongside Horologium I, Reticulum II, Segue 1, Draco II, and Tucana II (Simon 2019). Specifically, Boo II can be classified as the third most metal-poor dwarf galaxy after Tucana II and Horologium I (Simon 2019).

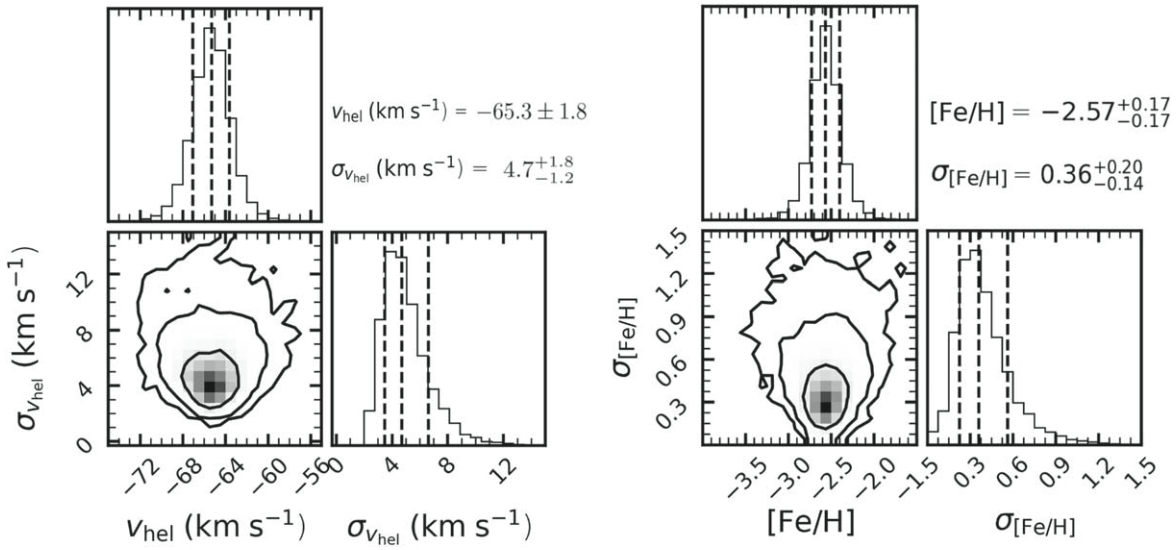

Figure 3. The resulting 2D posterior probability distributions from running an MCMC sampler and likelihood function as outlined in Section 4.1 for Aqu II. In the 1D histogram, the dashed lines display the 16th, 50th, and 84th percentiles, while the 2D histogram contours display the 68%, 95.5%, and 99.7% confidence intervals from the peak density. Left: the resulting distribution for the systemic velocity (v_{hel}) and velocity dispersion ($\sigma_{v_{hel}}$). Right: the resulting distribution for the systemic metallicity ([Fe/H]) and metallicity dispersion ($\sigma_{[Fe/H]}$).

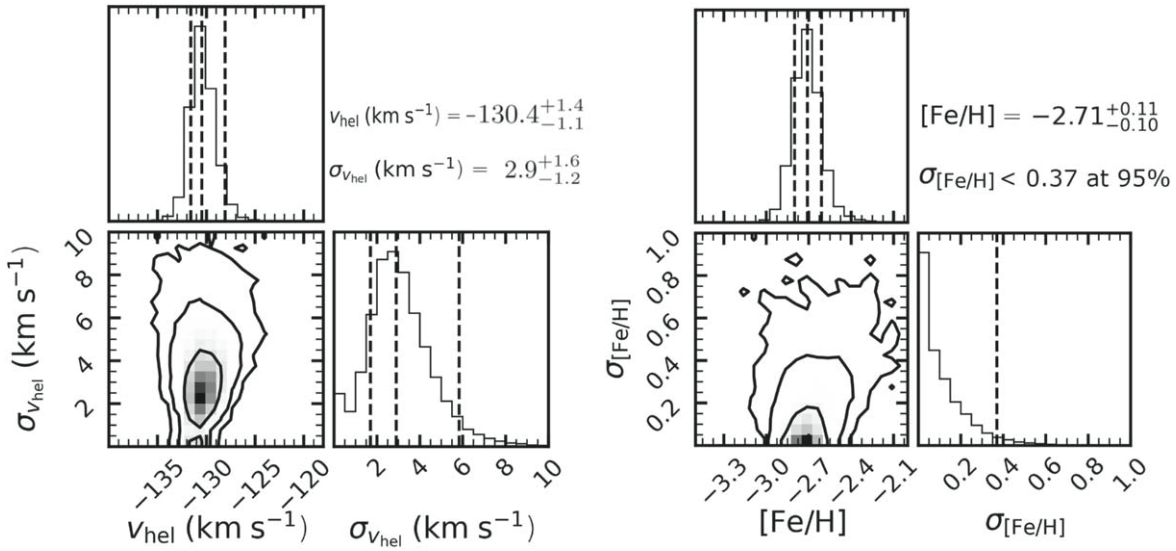

Figure 4. The resulting 2D posterior probability distributions from running an MCMC sampler and likelihood function as outlined in Section 4.1 for Boo II. Left: the resulting distribution for the systemic velocity (v_{hel}) and velocity dispersion ($\sigma_{v_{hel}}$). In the 1D histogram. the dashed lines display the 16th, 50th, and 84th percentiles, while the 2D histogram contours display the 68%, 95.5%, and 99.7% confidence intervals from the peak density. Right: the resulting distribution for the systemic metallicity ([Fe/H]) and metallicity dispersion ($\sigma_{[Fe/H]}$). In the upper-left 1D histogram the dashed lines display the 16th, 50th, and 84th percentiles, while the dashed line in the lower-right 1D histogram displays the 95th percentile location. The contour lines in the 2D histogram display the 68%, 95.5%, and 99.7% confidence intervals from the peak density.

4.2. Dynamical Mass and Mass-to-light Ratio

As described in Wolf et al. (2010), assuming both Aqu II and Boo II are in dynamical equilibrium, we can use their resolved velocity dispersions to estimate the system's enclosed mass within 1 $r_{1/2}$ using the relation

$$M_{1/2} \approx 930 \left(\frac{\langle \sigma^2_{v_{hel}} \rangle}{\mathrm{km^2\ s^{-2}}} \right) \left(\frac{r_{1/2}}{\mathrm{pc}} \right) M_\odot. \quad (2)$$

We used the reported half-light radii from Torrealba et al. (2016) for Aqu II and Muñoz et al. (2018) for Boo II, respectively. Additionally, we treat these half-light radii and the previously determined velocity dispersions from Section 4.1 as Gaussians with a mean of their systemic value and a standard deviation of their uncertainty. We then sampled the estimation relation (Equation (2)) 1000 times using these Gaussians, and report the median as the systemic mass and the 16th and 84th percentiles as the uncertainties. We then estimate the mass-to-light ratio using the absolute V-band magnitude (M_V) from Torrealba et al. (2016) for Aqu II and Muñoz et al. (2018) for Boo II.

For Aqu II, we estimated a dynamical half-light mass of $3.1^{+3.0}_{-1.4} \times 10^6 M_\odot$, and a mass-to-light ratio of $1300^{+1300}_{-600} M_\odot / L_\odot$. This large mass-to-light ratio distinctly indicates the dark-matter-

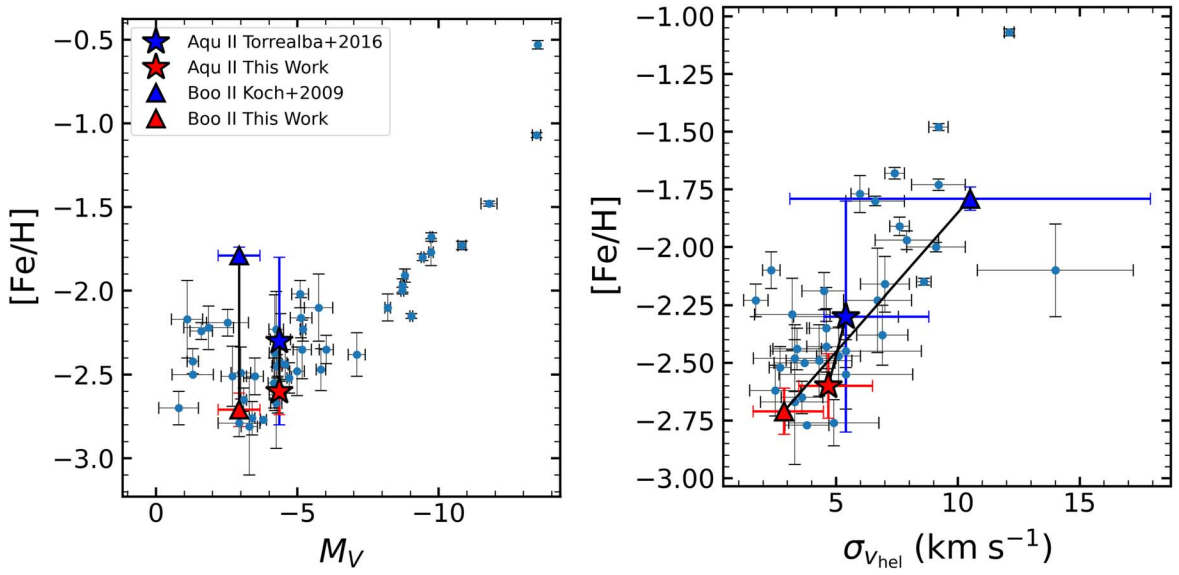

Figure 5. Left: comparison of systemic metallicity ([Fe/H]) as a function of absolute V-band magnitude (M_V) from this work and previous literature measurements for both UFDs. Right: a comparison of the systemic metallicity ([Fe/H]) as a function of velocity dispersion ($\sigma_{v_{hel}}$). The properties of all known UFDs are shown as blue dots using the luminosities and velocity dispersions from Pace et al. (2022) and the metallicities from Simon (2019) (a full list of references can be found in Appendix). The values reported in this work agree with the trend of other UFDs, resolving the inconsistency presented by the previous Boo II literature velocity dispersion.

dominated nature of Aqu II, as expected due to its identity as a UFD. For Boo II, we estimate a dynamical half-mass of $3.1^{+4.4}_{-2.1} \times 10^5 M_\odot$, and a mass-to-light ratio of $460^{+1000}_{-440} M_\odot/L_\odot$. Boo II is therefore consistent with a large dark matter content, as well, but we cannot confirm at high confidence that it is dark matter dominated because of the large uncertainties. These large uncertainties, as well as the unresolved metallicity dispersion, prevent us from explicitly ruling out the identity of Boo II as a GC. However, given the large half-light radius of $r_{1/2} = 38.7 \pm 5.1$ pc and the velocity dispersion of $v_{hel} = 2.9^{+1.6}_{-1.2}$ km s^{-1}, it is more likely to be a UFD. Using Equation (2) and assuming a mass-to-light ratio of 3, the predicted velocity dispersion for a GC would be $\sim$0.23 km s^{-1}. This is more than 10 times smaller than what we measure. Ji et al. (2016b) also suggests that the metallicity distribution of Boo II is similar to that of other UFDs. In addition, the neutron-capture elements have very low abundance limits, which is consistent with observations of other UFDs and generally not consistent with the abundance patterns observed in GCs. Furthermore, the metallicity, velocity dispersion, luminosity, and orbital characteristics of Boo II are also consistent with other UFDs as seen in Figures 5 and 7.

4.3. Literature Comparison in Spectroscopic Members

The increased sample size of confirmed bright RGB members provides smaller uncertainties and significant improvements to the systemic velocities, velocity dispersions, metallicities, and dynamical mass estimates of Aqu II and Boo II. In Figure 5, we show the comparison of the metallicity and velocity dispersions from this work with previous measurements from the literature on these two UFDs.

Torrealba et al. (2016) provides the most recent measurements for Aqu II, using nine member stars (four RGB and five BHB) to report a systemic velocity $v_{hel} = -71.1 \pm 2.5$ km s^{-1} with a dispersion $\sigma_{v_{hel}} = 5.4^{+3.4}_{-0.9}$ km s^{-1}, generating a mass estimate $2.7^{+6.6}_{-0.5} \times 10^6 M_\odot$, a metallicity [Fe/H] $= -2.3 \pm 0.5$, and no resolved metallicity dispersion. We measured a systemic velocity difference of $\sim$6 km s^{-1} at $v_{hel} = -65.3 \pm 1.8$ km s^{-1}, with a 28% smaller uncertainty. Despite the slightly larger sample size in Torrealba et al. (2016) of nine stars, our increased precision most likely originates from our sample of RGB stars rather than BHB stars. These BHB stars have a fainter magnitude and broader absorption-line features and therefore a larger velocity uncertainty. Similarly, we resolve a smaller velocity dispersion at $\sigma_{v_{hel}} = 4.7^{+1.8}_{-1.2}$, with the upper error decreased by almost a factor of 2. Most noticeably, however, we measure an average metallicity 0.27 dex lower, at [Fe/H] $= -2.57^{+0.17}_{-0.17}$, with an uncertainty smaller by a factor of 3. This decreased average metallicity further identifies the extremely metal-poor nature of Aqu II. Furthermore, while Torrealba et al. (2016) does not report a metallicity dispersion, we are able to resolve it due to our RGB sample size. This dispersion at [Fe/H] $= 0.36^{+0.20}_{-0.14}$ further displays the spread of metallicity among members and highlights the nature of Aqu II as a UFD.

Using the GMOS-N spectrograph on the Gemini North Telescope, the spectral resolution of which is $R \sim 4000$, Koch et al. (2009) provided the first spectroscopic study of Boo II. Using five RGB members, Koch et al. (2009) reports a mean systemic velocity $v_{hel} = -117.0 \pm 5.2$ km s^{-1} with an extremely large dispersion $\sigma_{v_{hel}} = 10.5 \pm 7.4$ km s^{-1}, and a mean metallicity [Fe/H] $= -1.79 \pm 0.05$ with a dispersion $\sigma_{[Fe/H]} = 0.14$. Contrastingly, the IMACS/Magellan spectrograph used in this study provided a resolution of more than double that ($R \sim 11{,}000$). This increased resolution, combined with our sample size more than doubling the number of confirmed RGB members, significantly affected the systemic properties and drastically reduced uncertainties.

The systemic velocity of Boo II measured in this work differed from Koch et al. (2009) by more than 10 km s^{-1} at $-130.4^{+1.4}_{-1.1}$ km s^{-1} while decreasing the uncertainty by a factor of 4. Similarly, we measure a decrease in the metallicity of Boo II by almost 1 dex, to $-2.71^{+0.11}_{-0.10}$. A main difference in the metallicity calculation is that Koch et al. (2009) used a CaT-to-

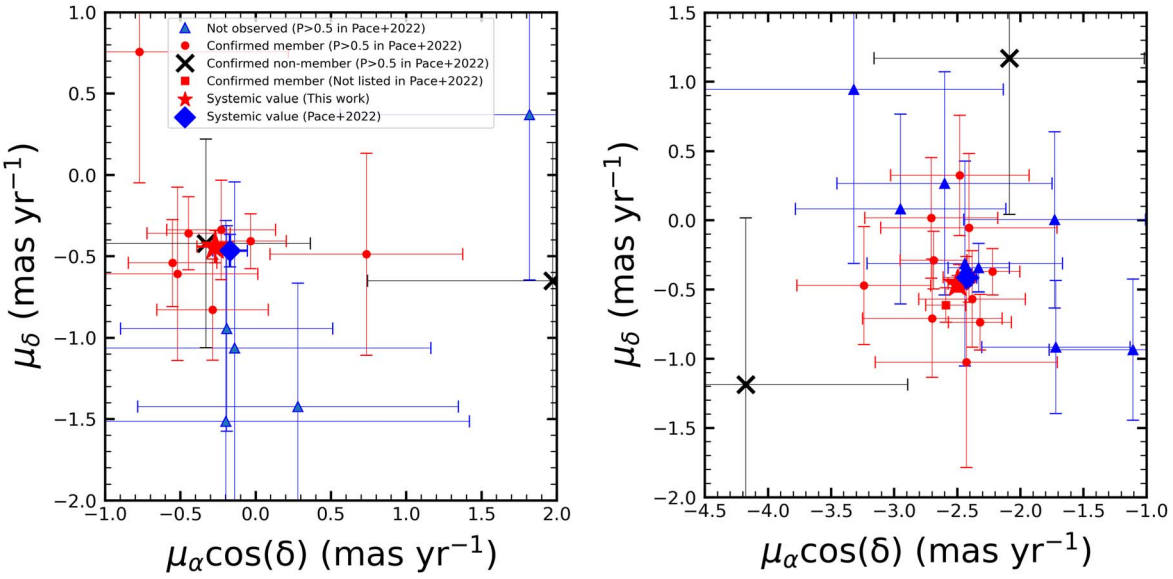

Figure 6. Comparison of member stars and systemic proper motion for Aqu II (left) and Boo II (right) between this work and Pace et al. (2022) using astrometry from Gaia DR3 (Gaia Collaboration et al. 2016, 2021; Lindegren et al. 2021). The systemic value for this work is the weighted average of spectroscopically confirmed member stars, while the systemic value from Pace et al. (2022) is from a mixture model based on photometric and astrometric data only.

metallicity conversion that was not calibrated for metallicities below [Fe/H] = −2. Carrera et al. (2013) later extended the conversion relation to [Fe/H] = −4 dex, and this extended relation is what was used in our study. The difference in the conversion relations used most likely accounts for the large difference in systemic metallicity between this work and Koch et al. (2009). Most notably, we measure a velocity dispersion of Boo II that is smaller by a factor of 3 at $2.9^{+1.6}_{-1.2}$ km s^{-1}, with an uncertainty smaller by a factor of 5. This decrease in velocity dispersion would significantly affect the mass estimation, and therefore the mass-to-light ratio, which were not measured by Koch et al. (2009). Our increased sample size and improved velocity measurements for each star were the main factor for this reduced velocity dispersion.

McConnachie & Côté (2010) hypothesized that the velocity dispersion in Boo II could be explained by the presence of binary stars. Due to their low intrinsic velocity dispersion (∼2−8 km s^{-1}), UFDs are susceptible to unidentified binary stars (McConnachie & Côté 2010; Minor et al. 2010; Pianta et al. 2022). In particular, small sample sizes ($N \lesssim 10$) are quite susceptible to the inflation of the velocity dispersion if only single-epoch velocity data are available (McConnachie & Côté 2010; Minor et al. 2010), as the initial spectroscopy of Boo II has demonstrated. As previously mentioned, Ji et al. (2016b) identified that one star of the five members in the Koch et al. (2009) sample was a spectroscopic binary and had inflated the velocity dispersion. Similarly, we identify a second plausible binary member star based on measurements from Koch et al. (2009) and this work (see Section 3.3). The larger sample size of members in this work is less vulnerable to binary stars (although with nine stars it remains a small size). We do, however, have multiepoch data by comparing observations in this work to older GMOS data that can be used to detect the presence of further binaries using methods from Minor et al. (2010). We note many UFDs have had binary stars identified with multiepoch data (e.g., Carina II, Grus I, and Grus II; Li et al. 2018b; Simon et al. 2020; Chiti et al. 2022) which has led to an inflated velocity dispersion in some other dwarf galaxies (e.g., Triangulum II; Kirby et al. 2015a, 2017; Buttry et al. 2022).

A separate study of Boo II by Ji et al. (2016b) used high-resolution spectroscopy to observe four bright RGB stars in order to measure the chemical abundances of the system. Simon (2019) used these results to report a metallicity of [Fe/H] $=-2.79^{+0.06}_{-0.10}$, consistent with the extremely metal-poor nature derived in this work. Additionally, Simon (2019) report a metallicity dispersion of $\sigma_{[Fe/H]} < 0.35$, which is very similar to the upper limit of $\sigma_{[Fe/H]} < 0.37$ measured in this work. However, Ji et al. (2016b) stated that their observations spanned a limited range and had a small sample size—half of what was considered in this work.

4.4. Proper Motion and Orbital Analysis

We measured the systemic proper motion of both UFDs through a weighted average of the eight Aqu II and 12 Boo II confirmed member stars using Gaia DR3 astrometry. We note that, in the case of Boo II, both the RRL star and the spectroscopic binaries are included in proper-motion calculations. For Aqu II, we measure $\mu_\alpha = -0.27 \pm 0.12$ mas yr^{-1} and $\mu_\delta = -0.44 \pm 0.10$ mas yr^{-1}, and for Boo II we measure $\mu_\alpha = -2.50 \pm 0.07$ mas yr^{-1} and $\mu_\delta = -0.46 \pm 0.06$ mas yr^{-1}.

In Figure 6, we compare the proper motion of Aqu II and Boo II member stars with the results from Pace et al. (2022). While Pace et al. (2022) contained a larger sample size of high-probability member candidates (seven more for Aqu II, nine more for Boo II), our proper-motion measurements were able to exclude nonmembers based on kinematic information from spectroscopy that was included in the measurements from Pace et al. (2022). In fact, we confirm that four high-probability member candidates (two in each UFD) in Pace et al. (2022) are nonmembers, which indeed slightly shifted the systemic proper motion.

These contaminant stars resemble members in both proper motion and photometry space, but are clearly nonmembers when observed in velocity space. By removing these contaminants, we determine a more robust measurement of

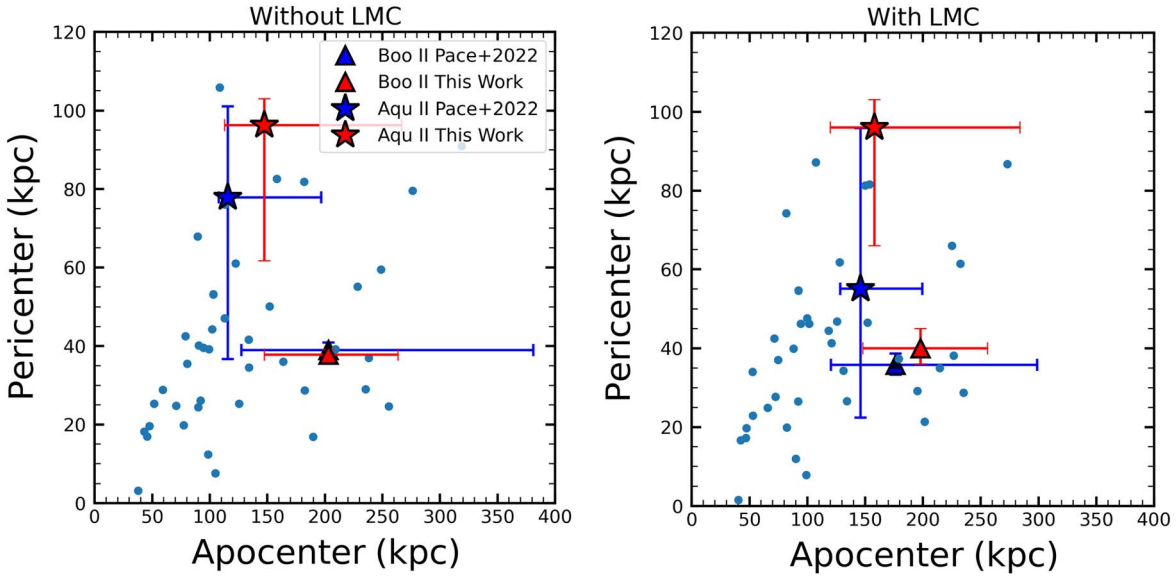

Figure 7. Comparison of orbital characteristics for both UFDs between this work and Pace et al. (2022), with all known UFDs displayed as blue dots using values from Pace et al. (2022). Left: comparison of the nearest apocenter and pericenter distances for both UFDs without the inclusion of the LMC. Right: comparison of the apocenter and pericenter distances for both UFDs with the inclusion of the LMC.

systemic proper motion, which in turn generates a more robust orbital analysis. We specifically note that the Boo II RRL member star (Gaia DR3 source ID: 3727826519650056576) is not included in Pace et al. (2022) but was spectroscopically confirmed as a member. This star is the second brightest member star (in g_0 magnitude) and has one of the most precise proper motions, resulting in it having a large influence on the systemic proper motion.

Our proper-motion measurements also generally agree within 1σ of additional studies using Gaia DR3 measurements (McConnachie & Venn 2020; Battaglia et al. 2022; Pace et al. 2022). The exceptions are that McConnachie & Venn (2020) reports a μ_α for Boo II consistent only within 2σ of the value in this work, and Battaglia et al. (2022) reports a μ_α for Aqu II only consistent within 2σ of this work.

We model the orbits using the 6D phase space (R.A., decl., distance, proper motion, and systemic velocity) parameters listed in Table 2 and `galpy` (Bovy 2015). We treat each trait as the mean of a Gaussian distribution with a standard deviation equal to the uncertainty and sample from them 1000 times. We integrate backwards in time 5 Gyr, recording the eccentricity and nearest apocenter and pericenter. The nearest apocenter or pericenter is described as being the first local minimum or maximum recorded in our orbit integration. The choice to make this constraint is motivated by the results of Pace et al. (2022) and D'Souza & Bell (2022), which highlight the unreliability of considering preceeding values. We also excluded instances where the orbit was unbound and resulted in no local minima or maxima being available. In this work, we initialized the 1000 orbits using the `McMillan17` gravitational potential (McMillan 2017), considering scenarios with and without the inclusion of the Large Magellanic Cloud (LMC) potential. When included, following the methods from Pace et al. (2022), the LMC potential has a Hernquist profile with a mass of $1.38 \times 10^{11}\ M_\odot$ (Erkal et al. 2019) and a scale radius of 16.09 kpc. This scale radius was chosen so that the mass of the profile within 8.7 kpc is consistent with the mass of $(1.7 \pm 0.7) \times 10^{10}\ M_\odot$ reported by van der Marel & Kallivayalil (2014).

In Figure 7, we show the orbital characteristics of these two UFDs along with all other known UFDs using values from Pace et al. (2022). For Aqu II, we measure a pericenter of 96^{+7}_{-35} kpc, an apocenter of 148^{+119}_{-35} kpc, and an eccentricity of $0.30^{+0.20}_{-0.11}$ without the inclusion of the LMC. When including the LMC, the pericenter remains at 96^{+7}_{-30} kpc, the apocenter increases to 158^{+126}_{-38} kpc, and the eccentricity increases to $0.32^{+0.18}_{-0.08}$.

For Boo II, we measure a pericenter of 38^{+1}_{-2} kpc, an apocenter of 203^{+61}_{-56} kpc, and an eccentricity of $0.69^{+0.06}_{-0.08}$ without the LMC potential. When including the LMC, the pericenter increases to 40^{+5}_{-4} kpc, the apocenter decreases to 198^{+58}_{-50} kpc, and the eccentricity decreases to $0.67^{+0.05}_{-0.07}$.

For Aqu II, Pace et al. (2022) reports a pericenter, apocenter, and eccentricity of $77.9^{+23.2}_{-41.2}$ kpc, $115.6^{+81.3}_{-7.8}$ kpc, and $0.31^{+0.24}_{-0.13}$, respectively, without inclusion of the LMC. Similarly for Boo II, they report a pericenter, apocenter, and eccentricty of 39.0 ± 1.9 kpc, $203.0^{+178.1}_{-75.4}$ kpc, and $0.68^{+0.10}_{-0.11}$ without the LMC, respectively. These values are consistent within 1σ of our spectroscopic member sample which utilized improved systemic velocity measurements and excluded contaminant stars affecting proper motions.

A study by Battaglia et al. (2022) used Gaia EDR3 values to model the orbits of 74 dwarf galaxies or dwarf galaxy candidates in the Local Group using multiple gravitational potentials. The values attained using the heavy model (a larger total virial mass than in `McMillan17`) for Boo II agree within 1σ of the measurements of this work. However, the values for Aqu II only agree within 2σ of the values in this work. Battaglia et al. (2022) also used a light model (a smaller virial mass than in `McMillan17`) to analyze Aqu II (but not Boo II), which generated a pericenter and apocenter that agreed within 1σ of the systemic values in this work; however, the eccentricity still only agreed within 2σ. The main reason for this inconsistency is most likely due to the our use of the `McMillan17` potential as opposed to the potentials used in Battaglia et al. (2022).

Another study, by Li et al. (2021), similarly uses data from Gaia EDR3 to estimate the proper motion and model the orbits of 46 dwarf galaxies in the Milky Way. Comparing the values from their model using the most massive Milky Way mass available (15×10^{11} $M_{\odot}$), the values for apocenter and pericenter of both Boo II and Aqu II are consistent within 1σ of the values measured in this work. The eccentricity for Boo II also agrees within 1σ of our measurements; however, the eccentricity of Aqu II only agrees within 2σ.

4.5. Astrophysical J-factor

The UFDs are an excellent target for searches of dark matter annihilation or decay due to their close distance, large dark matter densities, and low astrophysical backgrounds (e.g., Baltz et al. 2008; Ackermann et al. 2015). The astrophysical component of the dark matter annihilation (decay) rate is referred to as the J-factor (D-factor) and depends on the squared (linear) dark matter density along the line of sight. To compute the dark matter density of Aqu II and Boo II, we follow the methodology in Pace & Strigari (2019). Briefly, we compute the line-of-sight velocity dispersion from the spherical Jeans equation and compare the solutions to the observed velocity dispersions to determine the dark matter distribution (e.g., Bonnivard et al. 2015; Geringer-Sameth et al. 2015). For the Jeans modeling, we assume a Navarro–Frenk–White profile (Navarro et al. 1996) for the dark matter, a Plummer profile for the stellar distribution, and that the stellar anisotopy is constant with radius. We assume Gaussian errors for the distance and structural parameters (r_h, ϵ); for additional details, see Pace & Strigari (2019).

We apply this framework to the eight-star sample of Aqu II and the nine-star sample of Boo II (removing the RRL and binary stars). For Aqu II, we find $\log_{10} J(\theta) = 17.5^{+0.6}_{-0.5}$, $17.7^{+0.6}_{-0.5}$, $17.8^{+0.6}_{-0.5}$, and $17.8^{+0.6}_{-0.6}$ for solid angles of $\theta = 0.1°$, $0.2°$, $0.5°$, and $1°$ in logarithmic units of GeV^2 cm^{-5}. With the same methodology, Pace & Strigari (2019) found $\log_{10} J(0°5) \sim 18.3$ with the Torrealba et al. (2016) data set. The difference is due to the larger velocity dispersion in the Torrealba et al. (2016) data set. For the D-factor of Aqu II, we find $\log_{10} D(\theta) = 16.9 \pm 0.3$, $17.3^{+0.4}_{-0.3}$, and $17.8^{+0.4}_{-0.5}$, for solid angles of $\theta = 0.1°$, $0.2°$, and $0.5°$ in logarithmic units of GeV cm^{-2}. For Boo II, we find $\log_{10} J(\theta) = 18.0^{+0.8}_{-1.1}$, $18.1^{+0.8}_{-1.1}$, $18.3^{+0.8}_{-1.1}$, and $18.4^{+0.8}_{-1.1}$ for solid angles of $\theta = 0.1°$, $0.2°$, $0.5°$, and $1°$. There is a small tail in the velocity dispersion toward low values, which leads to a similar low-value tail in the J-factor. We note if we reject values below $\log_{10} J = 16.5$, then the median J-factor increases by $\sim$0.1. For the D-factor of Boo II, we find $\log_{10} D(\theta) = 16.9^{+0.5}_{-0.6}$, $17.4^{+0.5}_{-0.6}$, and $17.9^{+0.6}_{-0.7}$, for solid angles of $\theta = 0.1°$, $0.2°$, and $0.5°$ in logarithmic units of GeV cm^{-2}. In the future, with a larger data set that fully resolves the dispersion, we expect the J-factor to be larger than the median value quoted here. Boo II has an intermediate J-factor and will be an important target for searches for dark matter annihilation. Aqu II will be useful for stacked analyses searching for dark matter annihilation products.

5. Conclusion

In this work, we present a refined study of two UFDs, Aqu II and Boo II, using medium-resolution spectroscopy obtained from Magellan/IMACS. With a high-efficiency target selection utilizing Gaia astrometry (Pace et al. 2022), we have roughly doubled the number of spectroscopic members in both UFDs.

With our larger samples, we provide precise systemic velocities, velocity dispersions, metallicities, metallicity dispersions, and orbital characteristics such as apocenters and pericenters. Most notably, we derive a velocity dispersion of Boo II that is not affected by the presence of a known binary star and a further suspected binary. Combining the removal of these binary stars with our improved stellar velocity measurements resulted in the velocity dispersion decreasing by a factor of 3. We also confirm the extremely metal-poor nature of both satellites ([Fe/H] < -2.50), making them two of the least metal-enriched dwarfs known. Additionally, based on the large mass-to-light ratio ($M_{\odot}/L_{\odot} \sim 1300$), we conclude that Aqu II is highly dark matter dominated. We do note that our observations are mostly focused on stars not previously observed, preventing us from testing for binary stars located in our sample (aside from the two binary stars described Table 5). Further observations of high-probability member candidates could improve upon this and provide opportunities for binarity to be tested and further increase the accuracy of our results.

These observations also show the high efficiency in target selection based on the high-probability member candidates constructed with the photometric and astrometric data from Pace et al. (2022). For both Aqu II and Boo II over 80% of these well-observed candidates turned out to be members when observed with sufficient S/N. There still remain five (eight) high-probability member candidates for Aqu II (Boo II) that can be prioritized in future spectroscopic follow ups due to this high membership success rate.

Acknowledgments

J.B. and T.S.L. acknowledge financial support from Natural Sciences and Engineering Research Council of Canada (NSERC) through grant No. RGPIN-2022-04794. A.B.P. is supported by NSF grant No. AST-1813881.

This paper includes data gathered with the 6.5 meter Magellan Telescopes located at Las Campanas Observatory, Chile.

This work has made use of data from the European Space Agency (ESA) mission Gaia (https://www.cosmos.esa.int/gaia), processed by the Gaia Data Processing and Analysis Consortium (DPAC, https://www.cosmos.esa.int/web/gaia/dpac/consortium). Funding for the DPAC has been provided by national institutions, in particular the institutions participating in the Gaia Multilateral Agreement.

The Legacy Surveys consist of three individual and complementary projects: the Dark Energy Camera Legacy Survey (DECaLS; NOAO Proposal ID #2014B-0404; PIs: David Schlegel and Arjun Dey), the Beijing-Arizona Sky Survey (BASS; NOAO Proposal ID #2015A-0801; PIs: Zhou Xu and Xiaohui Fan), and the Mayall z-band Legacy Survey (MzLS; NOAO Proposal ID #2016A-0453; PI: Arjun Dey). DECaLS, BASS, and MzLS together include data obtained, respectively, at the Blanco Telescope, Cerro Tololo Inter-American Observatory, National Optical Astronomy Observatory (NOAO); the Bok Telescope, Steward Observatory, University of Arizona; and the Mayall Telescope, Kitt Peak National Observatory, NOAO. The Legacy Surveys project is honored to be permitted to conduct astronomical research on

Iolkam Du'ag (Kitt Peak), a mountain with particular significance to the Tohono O'odham Nation.

NOAO is operated by the Association of Universities for Research in Astronomy (AURA) under a cooperative agreement with the National Science Foundation.

This project used data obtained with the Dark Energy Camera (DECam), which was constructed by the DES collaboration. Funding for the DES Projects has been provided by the US Department of Energy, the US National Science Foundation, the Ministry of Science and Education of Spain, the Science and Technology Facilities Council of the United Kingdom, the Higher Education Funding Council for England, the National Center for Supercomputing Applications at the University of Illinois at Urbana-Champaign, the Kavli Institute of Cosmological Physics at the University of Chicago, Center for Cosmology and Astro-Particle Physics at the Ohio State University, the Mitchell Institute for Fundamental Physics and Astronomy at Texas A&M University, Financiadora de Estudos e Projetos, Fundação Carlos Chagas Filho de Amparo, Financiadora de Estudos e Projetos, Fundação Carlos Chagas Filho de Amparo á Pesquisa do Estado do Rio de Janeiro, Conselho Nacional de Desenvolvimento Cientifico e Tecnologico and the Ministerio da Ciencia, Tecnologia e Inovacao, the Deutsche Forschungsgemeinschaft and the Collaborating Institutions in the Dark Energy Survey. The Collaborating Institutions are Argonne National Laboratory, the University of California at Santa Cruz, the University of Cambridge, Centro de Investigaciones Energeticas, Medioambientales y Tecnologicas-Madrid, the University of Chicago, University College London, the DES-Brazil Consortium, the University of Edinburgh, the Eidgenossische Technische Hochschule (ETH) Zurich, Fermi National Accelerator Laboratory, the University of Illinois at Urbana-Champaign, the Institut de Ciencies de l'Espai (IEEC/CSIC), the Institut de Fisica d'Altes Energies, Lawrence Berkeley National Laboratory, the Ludwig-Maximilians Universitat Munchen, and the associated Excellence Cluster Universe, the University of Michigan, the National Optical Astronomy Observatory, the University of Nottingham, the Ohio State University, the University of Pennsylvania, the University of Portsmouth, SLAC National Accelerator Laboratory, Stanford University, the University of Sussex, and Texas A&M University.

BASS is a key project of the Telescope Access Program (TAP), which has been funded by the National Astronomical Observatories of China, the Chinese Academy of Sciences (the Strategic Priority Research Program "The Emergence of Cosmological Structures," grant No. XDB09000000), and the Special Fund for Astronomy from the Ministry of Finance. The BASS is also supported by the External Cooperation Program of Chinese Academy of Sciences (grant No. 114A11KYSB20160057), and the Chinese National Natural Science Foundation (grant No. 11433005).

The Legacy Survey team makes use of data products from the Near-Earth Object Wide-field Infrared Survey Explorer (NEOWISE), which is a project of the Jet Propulsion Laboratory/California Institute of Technology. NEOWISE is funded by the National Aeronautics and Space Administration.

The Legacy Surveys imaging of the DESI footprint is supported by the Director, Office of Science, Office of High Energy Physics of the US Department of Energy under contract No. DE-AC02-05CH1123; by the National Energy Research Scientific Computing Center, a DOE Office of Science User Facility under the same contract; and by the US National Science Foundation, Division of Astronomical Sciences under contract No. AST-0950945 to NOAO.

Appendix
References for Dwarf Galaxy Data in Figures 5 and 7

Here we provide a list the references for the velocity dispersions, metallicities, and luminosities of the dwarf galaxies plotted in Figure 5: Majewski et al. (2003), Battaglia et al. (2006), Simon & Geha (2007), Bellazzini et al. (2008), de Jong et al. (2008), Mateo et al. (2008), Okamoto et al. (2008), Koch et al. (2009), Walker et al. (2009a), Walker et al. (2009b), Simon et al. (2011), Willman et al. (2011), Fabrizio et al. (2012), Kirby et al. (2013a), Kirby et al. (2013b), Frebel et al. (2014), Bechtol et al. (2015), Drlica-Wagner et al. (2015), Koposov et al. (2015), Kim et al. (2015), Kirby et al. (2015b), Simon et al. (2015), Crnojević et al. (2016), Ji et al. (2016a), Kim et al. (2016), Torrealba et al. (2016), Torrealba et al. (2016), Collins et al. (2017), Caldwell et al. (2017), Kirby et al. (2017), Li et al. (2017), Mucciarelli et al. (2017), Simon et al. (2017), Spencer et al. (2017), Chiti et al. (2018), Koposov et al. (2018), Longeard et al. (2018), Li et al. (2018b), Muñoz et al. (2018), Mutlu-Pakdil et al. (2018), Torrealba et al. (2018), Simon (2019), Simon et al. (2020), Jenkins et al. (2021), Longeard et al. (2021), Chiti et al. (2023), and Cerny et al. (2023).

ORCID iDs

Ting S. Li https://orcid.org/0000-0002-9110-6163
Andrew B. Pace https://orcid.org/0000-0002-6021-8760
Mairead Heiger https://orcid.org/0000-0002-2446-8332
Ying-Yi Song https://orcid.org/0000-0002-6270-8851
Joshua D. Simon https://orcid.org/0000-0002-4733-4994

References

Ackermann, M., Albert, A., Anderson, B., et al. 2015, PhRvL, 115, 231301
Ahn, C. P., Alexandroff, R., Allende Prieto, C., et al. 2012, ApJS, 203, 21
Baltz, E. A., Berenji, B., Bertone, G., et al. 2008, JCAP, 2008, 013
Battaglia, G., Taibi, S., Thomas, G. F., & Fritz, T. K. 2022, A&A, 657, A54
Battaglia, G., Tolstoy, E., Helmi, A., et al. 2006, A&A, 459, 423
Bechtol, K., Drlica-Wagner, A., Balbinot, E., et al. 2015, ApJ, 807, 50
Bellazzini, M., Ibata, R. A., Chapman, S. C., et al. 2008, AJ, 136, 1147
Bonnivard, V., Combet, C., Daniel, M., et al. 2015, MNRAS, 453, 849
Bovill, M. S., & Ricotti, M. 2009, ApJ, 693, 1859
Bovy, J. 2015, ApJS, 216, 29
Bovy, J., Bahmanyar, A., Fritz, T. K., & Kallivayalil, N. 2016, ApJ, 833, 31
Brown, T. M., Tumlinson, J., Geha, M., et al. 2012, ApJL, 753, L21
Brown, T. M., Tumlinson, J., Geha, M., et al. 2014, ApJ, 796, 91
Buttry, R., Pace, A. B., Koposov, S. E., et al. 2022, MNRAS, 514, 1706
Caldwell, N., Walker, M. G., Mateo, M., et al. 2017, ApJ, 839, 20
Carrera, R., Pancino, E., Gallart, C., & del Pino, A. 2013, MNRAS, 434, 1681
Cerny, W., Simon, J. D., Li, T. S., et al. 2023, ApJ, 942, 111
Chiti, A., Frebel, A., Ji, A. P., et al. 2018, ApJ, 857, 74
Chiti, A., Frebel, A., Ji, A. P., et al. 2023, AJ, 165, 55
Chiti, A., Simon, J. D., Frebel, A., et al. 2022, ApJ, 939, 41
Clementini, G., Ripepi, V., Garofalo, A., et al. 2022, arXiv:2206.06278
Collins, M. L. M., Tollerud, E. J., Sand, D. J., et al. 2017, MNRAS, 467, 573
Cooper, M. C., Newman, J. A., Davis, M., Finkbeiner, D. P., & Gerke, B. F. 2012, spec2d: DEEP2 DEIMOS Spectral Pipeline, Astrophysics Source Code Library, ascl:1203.003
Crnojević, D., Sand, D. J., Zaritsky, D., et al. 2016, ApJL, 824, L14
DES Collaboration, Abbott, T. M. C., Abdalla, F. B., et al. 2018, ApJS, 239, 18
de Jong, J. T. A., Harris, J., Coleman, M. G., et al. 2008, ApJ, 680, 1112
Dey, A., Schlegel, D. J., Lang, D., et al. 2019, AJ, 157, 168
Dotter, A., Chaboyer, B., Jevremović, D., et al. 2008, ApJS, 178, 89
Dressler, A., Bigelow, B., Hare, T., et al. 2011, PASP, 123, 288

Drlica-Wagner, A., Bechtol, K., Rykoff, E. S., et al. 2015, ApJ, 813, 109
Drlica-Wagner, A., Carlin, J. L., Nidever, D. L., et al. 2021, ApJS, 256, 2
D'Souza, R., & Bell, E. F. 2022, MNRAS, 512, 739
Erkal, D., Belokurov, V., Laporte, C. F. P., et al. 2019, MNRAS, 487, 2685
Fabrizio, M., Merle, T., Thévenin, F., et al. 2012, PASP, 124, 519
Foreman-Mackey, D., Hogg, D. W., Lang, D., & Goodman, J. 2013, PASP, 125, 306
Frebel, A., Simon, J. D., & Kirby, E. N. 2014, ApJ, 786, 74
Gaia Collaboration, Brown, A. G. A., Vallenari, A., et al. 2021, A&A, 649, A1
Gaia Collaboration, Prusti, T., de Bruijne, J. H. J., et al. 2016, A&A, 595, A1
Gaia Collaboration, Vallenari, A., Brown, A. G. A., et al. 2022, arXiv:2208.00211
Gallart, C., Monelli, M., Ruiz-Lara, T., et al. 2021, ApJ, 909, 192
Geringer-Sameth, A., Koushiappas, S. M., & Walker, M. 2015, ApJ, 801, 74
Harris, W. E. 2010, arXiv:1012.3224
Hayashi, K., Chiba, M., & Ishiyama, T. 2020, ApJ, 904, 45
Jenkins, S. A., Li, T. S., Pace, A. B., et al. 2021, ApJ, 920, 92
Ji, A. P., Frebel, A., Simon, J. D., & Chiti, A. 2016a, ApJ, 830, 93
Ji, A. P., Frebel, A., Simon, J. D., & Geha, M. 2016b, ApJ, 817, 41
Kim, D., Jerjen, H., Geha, M., et al. 2016, ApJ, 833, 16
Kim, D., Jerjen, H., Mackey, D., Da Costa, G. S., & Milone, A. P. 2015, ApJL, 804, L44
Kirby, E. N., Boylan-Kolchin, M., Cohen, J. G., et al. 2013a, ApJ, 770, 16
Kirby, E. N., Cohen, J. G., Guhathakurta, P., et al. 2013b, ApJ, 779, 102
Kirby, E. N., Cohen, J. G., Simon, J. D., et al. 2017, ApJ, 838, 83
Kirby, E. N., Cohen, J. G., Simon, J. D., & Guhathakurta, P. 2015a, ApJL, 814, L7
Kirby, E. N., Simon, J. D., & Cohen, J. G. 2015b, ApJ, 810, 56
Koch, A., & Rich, R. M. 2014, ApJ, 794, 89
Koch, A., Wilkinson, M. I., Kleyna, J. T., et al. 2009, ApJ, 690, 453
Koposov, S. E., Casey, A. R., Belokurov, V., et al. 2015, ApJ, 811, 62
Koposov, S. E., Walker, M. G., Belokurov, V., et al. 2018, MNRAS, 479, 5343
Li, H., Hammer, F., Babusiaux, C., et al. 2021, ApJ, 916, 8
Li, T. S., Simon, J. D., Drlica-Wagner, A., et al. 2017, ApJ, 838, 8
Li, T. S., Simon, J. D., Kuehn, K., et al. 2018a, ApJ, 866, 22
Li, T. S., Simon, J. D., Pace, A. B., et al. 2018b, ApJ, 857, 145
Lindegren, L., Klioner, S. A., Hernández, J., et al. 2021, A&A, 649, A2
Longeard, N., Martin, N., Ibata, R. A., et al. 2021, MNRAS, 503, 2754
Longeard, N., Martin, N., Starkenburg, E., et al. 2018, MNRAS, 480, 2609
Majewski, S. R., Skrutskie, M. F., Weinberg, M. D., & Ostheimer, J. C. 2003, ApJ, 599, 1082
Mateo, M., Olszewski, E. W., & Walker, M. G. 2008, ApJ, 675, 201
McConnachie, A. W., & Côté, P. 2010, ApJL, 722, L209
McConnachie, A. W., & Venn, K. A. 2020, RNAAS, 4, 229
McMillan, P. J. 2017, MNRAS, 465, 76
Minor, Q. E., Martinez, G., Bullock, J., Kaplinghat, M., & Trainor, R. 2010, ApJ, 721, 1142
Mucciarelli, A., Bellazzini, M., Ibata, R., et al. 2017, A&A, 605, A46
Muñoz, R. R., Côté, P., Santana, F. A., et al. 2018, ApJ, 860, 66
Mutlu-Pakdil, B., Sand, D. J., Carlin, J. L., et al. 2018, ApJ, 863, 25
Mutlu-Pakdil, B., Sand, D. J., Crnojević, D., et al. 2021, ApJ, 918, 88
Navarro, J. F., Frenk, C. S., & White, S. D. M. 1996, ApJ, 462, 563
Oemler, A., Clardy, K., Kelson, D., Walth, G., & Villanueva, E. 2017, COSMOS: Carnegie Observatories System for MultiObject Spectroscopy, Astrophysics Source Code Library, ascl:1705.001
Okamoto, S., Arimoto, N., Yamada, Y., & Onodera, M. 2008, A&A, 487, 103
Pace, A. B., Erkal, D., & Li, T. S. 2022, ApJ, 940, 136
Pace, A. B., & Strigari, L. E. 2019, MNRAS, 482, 3480
Pianta, C., Capuzzo-Dolcetta, R., & Carraro, G. 2022, ApJ, 939, 3
Safarzadeh, M., & Spergel, D. N. 2020, ApJ, 893, 21
Schlafly, E. F., & Finkbeiner, D. P. 2011, ApJ, 737, 103
Shanks, T., Metcalfe, N., Chehade, B., et al. 2015, MNRAS, 451, 4238
Simon, J. D. 2019, ARA&A, 57, 375
Simon, J. D., Drlica-Wagner, A., Li, T. S., et al. 2015, ApJ, 808, 95
Simon, J. D., & Geha, M. 2007, ApJ, 670, 313
Simon, J. D., Geha, M., Minor, Q. E., et al. 2011, ApJ, 733, 46
Simon, J. D., Li, T. S., Drlica-Wagner, A., et al. 2017, ApJ, 838, 11
Simon, J. D., Li, T. S., Erkal, D., et al. 2020, ApJ, 892, 137
Spencer, M. E., Mateo, M., Walker, M. G., et al. 2017, AJ, 153, 254
Strigari, L. E. 2018, RPPh, 81, 056901
Tarumi, Y., Yoshida, N., & Frebel, A. 2021, ApJL, 914, L10
Torrealba, G., Belokurov, V., Koposov, S. E., et al. 2018, MNRAS, 475, 5085
Torrealba, G., Koposov, S. E., Belokurov, V., et al. 2016, MNRAS, 463, 712
Torrealba, G., Koposov, S. E., Belokurov, V., & Irwin, M. 2016, MNRAS, 459, 2370
van der Marel, R. P., & Kallivayalil, N. 2014, ApJ, 781, 121
Walker, M. G., Mateo, M., Olszewski, E. W., et al. 2006, AJ, 131, 2114
Walker, M. G., Mateo, M., & Olszewski, E. W. 2009a, AJ, 137, 3100
Walker, M. G., Mateo, M., Olszewski, E. W., et al. 2009b, ApJ, 704, 1274
Walsh, S. M., Jerjen, H., & Willman, B. 2007, ApJL, 662, L83
Walsh, S. M., Willman, B., Sand, D., et al. 2008, ApJ, 688, 245
Weisz, D. R., Dolphin, A. E., Skillman, E. D., et al. 2014, ApJ, 789, 148
Willman, B., Geha, M., Strader, J., et al. 2011, AJ, 142, 128
Wolf, J., Martinez, G. D., Bullock, J. S., et al. 2010, MNRAS, 406, 1220
Zaritsky, D., & Behroozi, P. 2023, MNRAS, 519, 871